HEAT TRANSFER AND FLOW MEASUREMENTS IN GAS TURBINE ENGINE CAN AND ANNULAR COMBUSTORS

Andrew C. Carmack

Thesis submitted to the faculty of the Virginia Polytechnic Institute and State University

in partial fulfillment of the requirements for the degree of

Master of Science

In

Mechanical Engineering

Srinath V. Ekkad

Brian Y. Lattimer

Walter F. O'Brien

April 25, 2012

Blacksburg, VA

Keywords: Combustor liner cooing, Swirler, Infrared Thermal Imaging, Dry Low Emission(DLE) combustors

HEAT TRANSFER AND FLOW MEASUREMENTS IN GAS TURBINE ENGINE CAN AND ANNULAR COMBUSTORS

Andrew C. Carmack

ABSTRACT

A comparison study between axial and radial swirler performance in a gas turbine can combustor was conducted by investigating the correlation between combustor flow field geometry and convective heat transfer at cold flow conditions for Reynolds numbers of 50,000 and 80,000. Flow velocities were measured using Particle Image Velocimetry (PIV) along the center axial plane and radial cross sections of the flow. It was observed that both swirlers produced a strong rotating flow with a reverse flow core. The axial swirler induced larger recirculation zones at both the backside wall and the central area as the flow exits the swirler, and created a much more uniform rotational velocity distribution. The radial swirler however, produced greater rotational velocity as well as a thicker and higher velocity reverse flow core. Wall heat transfer and temperature measurements were also taken. Peak heat transfer regions directly correspond to the location of the flow as it exits each swirler and impinges on the combustor liner wall.

Convective heat transfer was also measured along the liner wall of a gas turbine annular combustor fitted with radial swirlers for Reynolds numbers 210000, 420000, and 840000. The impingement location of the flow exiting from the radial swirler resulted in peak heat transfer regions along the concave wall of the annular combustor. The convex side showed peak heat transfer regions above and below the impingement area. This behavior is due to the recirculation zones caused by the interaction between the swirlers inside the annulus.

ACKNOWLEDGEMENTS

I would like to sincerely thank Dr. Srinath V. Ekkad for being my advisor and giving me the opportunity to attend graduate school. His guidance and motivation has given me the confidence and strength to succeed in my studies. I would also like to express my gratitude to Solar Turbines for funding me during my time in graduate school.

Thank you as well to all my friends and roommates for the unforgettable times we've had in all of our years here at Virginia Tech. I would also like to thank my lab mates, particularly Justin Lamont, Christopher LeBlanc, Dr. Diganta Narzary, and Arnab Roy for their assistance with my research and studies. Thank you all for the memories and lifelong friendships.

Finally, I would like to thank my parents Clare and Dale Carmack for the guidance and inspiration they have given me over the years. Your love and support for me has made me who I am today.

TABLE OF CONTENTS

LIST OF FIGURES

NOMENCLATURE

S_n swirl number

G_m axial flux of angular momentum

D_{sw} outer swirler diameter

G_t axial thrust

Re Reynolds number

ρ fluid density

u mean flow velocity

D characteristic length

μ (absolute) dynamic fluid viscosity

Nu Nusselt number (hD/k)

h convective heat transfer coefficient

k thermal conductivity of the fluid

R(s) spatial correlation

I_1 pixel intensity of first image in image pair

I_2 pixel intensity of second image in image pair

X pixel location in image pair

$\langle \boldsymbol{I} \rangle$ mean image intensity

I' intensity fluctuation

Q constant wall heat flux

Q_{loss} estimated conduction heat loss

A surface area of the heater

T_{wall} measured wall temperature

T_{air} mainstream air temperature

V voltage input to surface heater

R electrical resistance of surface heater

CHAPTER 1: INTRODUCTION

Gas turbine engines have been used over the years as a useful source for vehicle propulsion and power generation. Air enters the engine through a compressor which increases the air pressure to achieve the proper conditions for combustion. The compressed air enters the combustion chamber where fuel is added and burned. The hot gasses from the combustor then pass through the turbine section of the engine, which is connected to a central shaft that links the compressor and turbine sections. A portion of the momentum from the hot combustion gasses is harnessed by the turbine blades to rotate the shaft, which resultantly turns the compressor and runs the engine.

One major topic of gas turbine research is on viable methods of improving fuel efficiency. It is known that a basic way to increase efficiency is to spin the engine faster. In order to do this, a higher burn temperature in the combustor must be achieved. Higher combustion temperatures, however, will produce larger amounts of pollutants. With the strict limitations of the modern day emission standards and the continuing desire for higher fuel efficiency in the gas turbine industry, it has become a growing importance for combustor design engineers to better understand the flow distribution within the combustor and the heat transfer process between the gas flow path and the combustor liner wall. With burn temperatures reaching levels higher than the melting point of the materials used to construct the combustors, the walls of the combustor must be cooled in order to prevent damage or failure. A detailed analysis of the combustor liner heat transfer will determine the necessary amount and location of cooling along the wall and will prevent any overcooled or undercooled regions. This will allow the combustor to run

at an optimal temperature for emissions and efficiency with minimal losses to the combustor liner.

This study focuses on comparing the flow field geometry and behavior with the combustor liner wall heat transfer inside a gas turbine engine can combustor equipped with both an inlet axial and radial swirler. The combustor liner wall heat transfer was also measured on both the concave and convex walls of a gas turbine engine annular combustor using inlet radial swirlers. These findings will help better understand the flow behavior inside the different combustors and ultimately design an effective cooling scheme for the combustor walls.

1.1 Liner Wall Cooling Systems

The combustor liner comprises the inner portion of the combustor that contains the combustion process. This exposes the liner to temperatures capable of exceeding the melting point of the liner material. Due to this occurrence, it is necessary to employ an effective cooling scheme while still maintaining the structural integrity of the liner. Various methods such as coating the walls with low conductance ceramic material known as a thermal barrier coating (TBC), or cooling techniques such as film cooling and back-side cooling have been studied and proven to be useful means of protecting the combustor from damage or failure. Figure 1.1 shows a typical film cooling scheme for a can combustor.

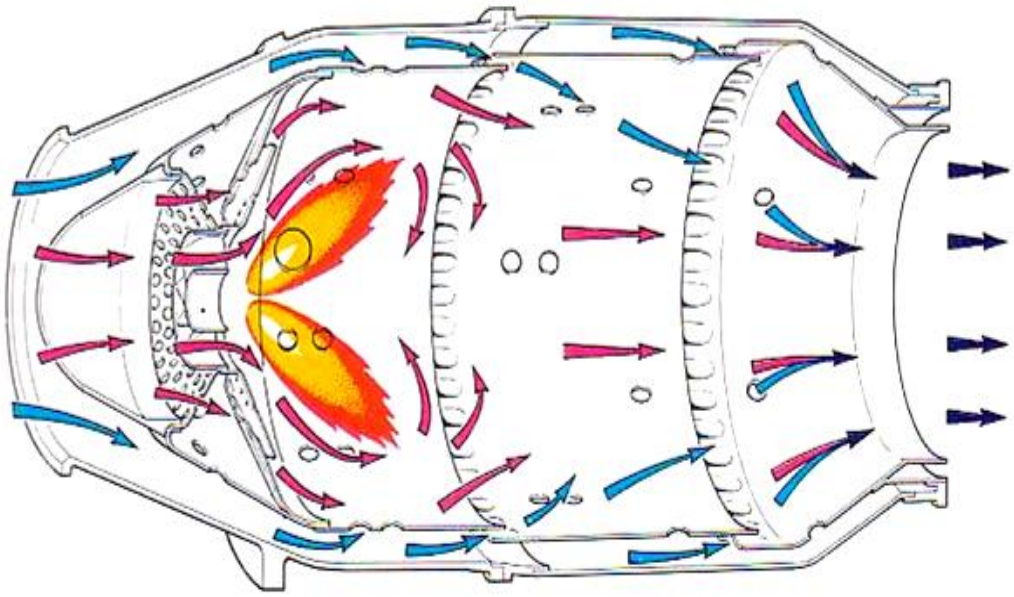

Figure 1.1. Combustor liner wall film cooling scheme [1**]**

In Figure 1.1, coolant air is injected into the combustor flow path via holes or slots in the combustor liner. This creates a thin film of cool air along the liner wall to regulate the wall temperature and prevent the liner from overheating. Proper design and regulation of

this cooling scheme is critical to the performance of the combustor. Too much coolant flow will result in wasted energy extracted by the turbine to provide the excessive coolant flow, as well as an overall decrease in the combustor temperature. This will resultantly decrease the fuel efficiency of the engine. If too little coolant is used then the combustor walls will overheat, which could lead to damage or destruction of the combustor. For these reasons, it is highly important for the combustor design engineer to understand the heat transfer profile along the combustor liner wall.

1.2 Pollutant Emissions

Pollutant emissions have been a widely researched topic, particularly in the last few decades as emission standards have become more stringent to protect the environment. Strict limitations have been placed on the allowable amount of oxides of nitrogen (NOx), carbon monoxide (CO), and unburned hydrocarbons (UHC) by the Environmental Protection Agency (EPA) as well as through the Clean Air Acts introduced by Congress. Production of these pollutants in gas turbine engines occurs from the incomplete combustion of the hydrocarbon based fuels and is directly affected by the burn temperature in the combustor. Figure 1.2 shows the relationship between pollutant production and the combustor primary zone temperature.

In Figure 1.2, it can be seen that the production of NOx shows an exponential growth as the combustor primary zone temperature is increased. Therefore, in order to decrease the production of NOx the combustor temperature must be decreased. However, the production of CO increases as the combustor primary zone temperature is decreased.

Because of this behavior, Figure 1.2 shows that the optimal temperature range for low emissions is roughly between 1670K and 1900K.

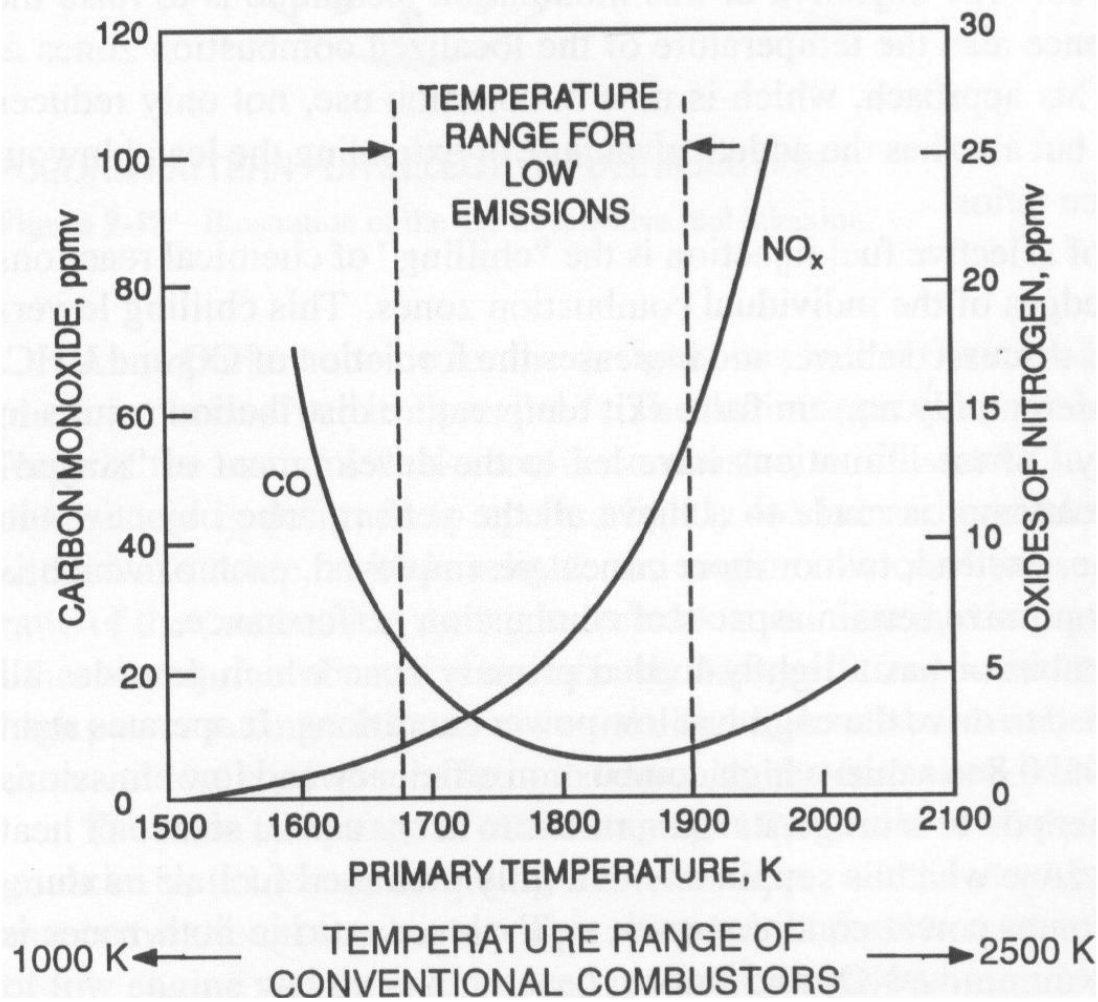

Figure 1.2. Relationship of the combustor primary zone temperature on the production of NOx and CO [2]

In order to maintain the combustion temperature ranges shown in Figure 1.2, the flame temperature must be carefully controlled. Ideally, the combustor would be regulated to have a radially uniform temperature that falls within the allowable temperature range. This would result in an acceptable mean burn temperature since there would be no fluctuation in the combustor temperature. However, an acceptable mean

burn temperature can also be seen in the case with large radial temperature fluctuations that produce very large high temperature zones and very low cool temperature zones. While the mean temperature falls in the allowable range, this case will still produce large amounts of NOx and CO and is therefore unacceptable. Thus, the engine should be properly designed for flame temperature regulation in order to eliminate the unacceptable large temperature gradients and help to create a more uniform temperature distribution within the combustor.

1.3 Solar Dry Low Emission (DLE) Combustor

A relatively new type of combustor called a Dry Low Emission (DLE) combustor has emerged as a reliable and effective design for reducing pollutant emissions. The "dry" term refers to the DLE combustor's ability to run without the injection of water or steam into the combustion chamber. The DLE combustor uses active control systems to regulate air-fuel flow through a complex array of injection nozzles. This allows the air fuel ratio (AFR) and combustion temperature to be properly controlled within a narrow band of 1500°C-1650°C flame temperatures. An example of a DLE combustor is the Solar Turbines MARS Low-NOx Combustor shown in Figure 1.3.

The Solar Turbines MARS Low-NOx Combustor shown in Figure 1.3 operates at different modes depending on the requested load. The DLE combustor operates similar to a standard combustor below 50% load. The DLE combustor enters its "low emissions mode" as the load increases above 50%. This means that the engine controls various bleed valves and inlet guide vanes to maintain combustor primary zone temperature in an acceptable range. [3]

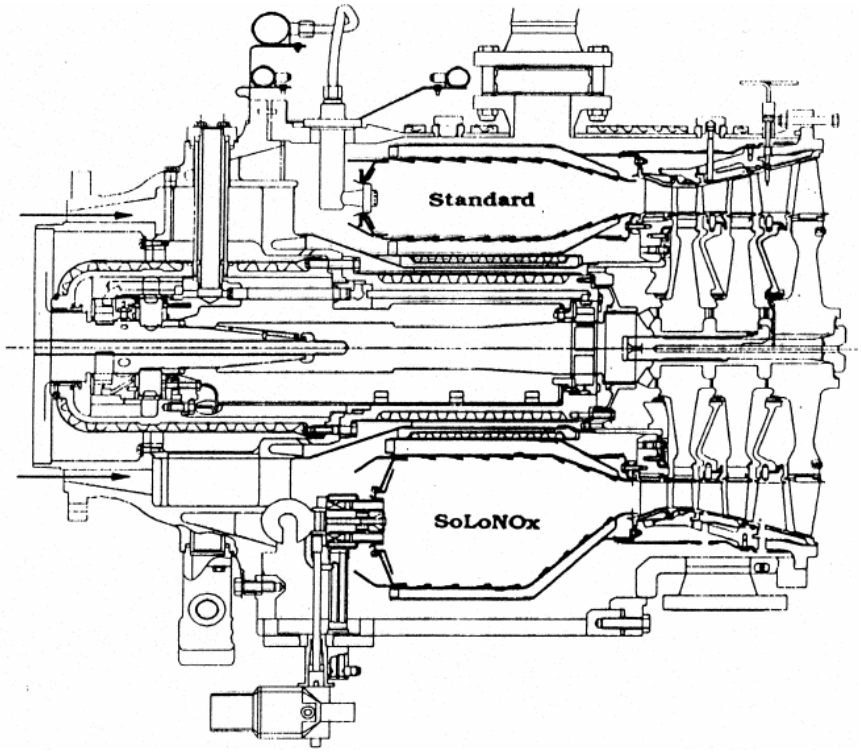

Figure 1.3. Solar Turbines MARS Low-NOx Combustor [1]

A comparison between a conventional burner and the Solar Turbines SoLoNOx combustor is shown in Figure 1.4

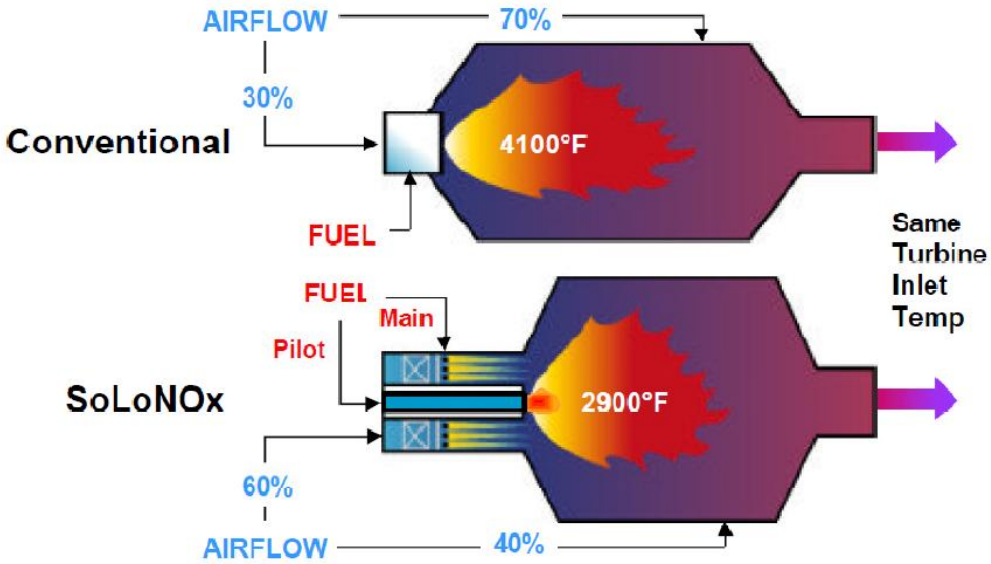

Figure 1.4. Comparison of conventional combustor to the Solar Turbines SoLoNOx[4**]**

In Figure 1.4, it can be seen that the Solar Turbines SoLoNOx combustor is able to produce the same turbine inlet temperature while operating at a much lower flame temperature. The shorter geometry of the SoLoNOx combustor provides less residence time inside the combustor, which effectively reduces NOx production. The SoloNOx combustor also uses 30% less of the inlet airflow for film cooling. This is preferable, as it is impractical to cool such large areas of the combustor with the limited coolant flow. The SoLoNOx combustor instead uses this 30% airflow for backside cooling and premixes the fuel to reduce local hot spots in the combustor flow path. [4]

With less air used for film cooling, the DLE combustors use focused cooling systems to cool the walls. These intelligent cooling systems provide the necessary amounts of coolant air along the wall and prevent any hot spots from forming. Figure 1.5 shows a diagram of a can combustor utilizing jet tubes along the combustor wall as opposed to the traditional film cooling holes.

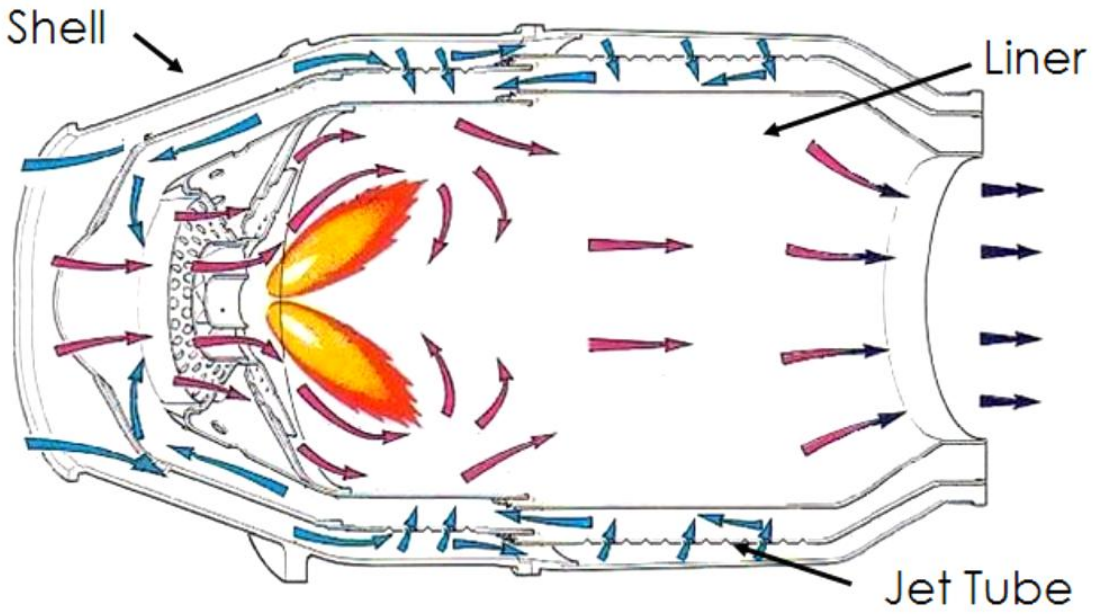

Figure 1.5. Can combustor with focused cooling [1]

1.4 Swirler

A common method of achieving a more uniform combustion temperature distribution and higher fuel efficiency is by fitting a swirler nozzle to the inlet to the combustion chamber. Swirlers are comprised of a set of stationary vanes that are set at an angle to turn the incoming air and induce heavy rotation in the flow in the combustor primary zone. Vane configurations can be aligned to induct air axially, as found in axial swirlers, or tangentially, as seen in radial swirlers. Fuel injectors are located inside the swirler and spray fuel into the rotating flow. The high degree of rotation caused by the swirler enhances air and fuel mixing which improves combustion fuel efficiency while reducing pollutant production. If the rotation is large enough, a low pressure core forms in the exiting flow from the swirler and can cause the core flow to move in the upstream direction while the outer flow continues downstream. This behavior is widely used to enhance mixing within the combustion chamber and can be designed to bring burnt combustion gasses back into the swirler. This gives the swirler the ability to act as a means of flame stabilization and a method of preheating the inlet airflow.

Swirlers can be characterized by a non-dimensional number called the swirl number. The swirl number is defined as:

$$S_n = 2G_m/(D_{sw}G_t) \tag{1.1}$$

where Gm is the axial flux of angular momentum, Gt is the axial thrust, and Dsw is the outer swirler diameter. The swirl number describes the strength of the rotation generated by the swirler. For swirl numbers less than 0.4, the flow is considered weak and the previously described reverse core flow will not occur. For swirl numbers greater than 0.6,

the flow is considered strong and will produce the reverse core flow. The majority of swirlers are designed for strong swirl.

1.5 Literature Survey

Multiple studies have been conducted on the effect of adding swirling flow generated by an inlet swirler to a gas turbine engine combustor on the combustor liner wall heat transfer. Goh [1] investigated the steady state wall heat transfer as well as the velocity flow field and turbulent intensity distributions inside a can combustor with an axial swirler. Abraham [3] conducted a study on both the steady state and transient wall heat transfer in a can combustor with an axial swirler. Sedalor [4] conducted a study on an annular combustion fitted with radial swirlers that focused the wall heat transfer at both concave and convex walls, as well as a CFD study on the velocity distributions inside the combustor.

Studies have also been carried out on different swirler designs. A typical swirler can be divided into three main design features; intake configuration, fuel injection method, and outlet geometry. The intake configuration is determined by the axial or radial orientation of the vanes and the desired degree of rotation that they produce. Other configurations as constructed by Pritchard, Jr et al [5] and Graves [6] involve sets of concentrically mounted swirlers, allowing separate rotation speeds of the inner and outer sections of the flow. In some cases vanes are substituted for angled slots or channels as seen in the studies of Auer et al. [7] and Xu et al. [8].

Various fuel injection methods have also been studied by King et al. [9, 10] where injectors were investigated at a central location with radial outward spray as well as

inside the vane passages. Studies by Andrews et al. [11, 12] have shown that a combination of the central radial outward and radial vane passage fuel injection locations can provide good flame stability for equivalence ratios as low as 0.1. The geometry of the fuel injectors can also be utilized for other purposes such as flow path guide lines or flame holding. Janus et al. [13] conducted tests on a radial swirler with a central fuel injector. The conically shaped fuel injector provided a guide for the flow to stabilize after passing through the swirler vanes. Abraham [3] and Patil et al. [14] investigated an axial swirler with bluff body fuel injectors located immediately downstream of the vanes. In this design, the air and fuel mixture is ignited and establishes a recirculation zone behind the bluff bodies that stabilizes the flame.

Outlet geometry design greatly influences the performance of swirlers. In the study by King et al. [10], outlet geometries of a standard flange, outlet shroud, and an outlet throat were tested to see the effect on velocity, equivalence ratio, combustion temperature, and pollutant production. The results showed that adding an outlet shroud to the standard flange increases the exit velocity from the swirler and creates a large recirculation zone along the wall. This design created a noticeably larger amount of combustion pollutants when compared to the standard flange without the shroud and the design with the outlet throat. The outlet throat design proved to be the most effective, as the added mixing length increased the uniformity of the equivalence ratio and thus significantly reduced pollutant emissions.

1.6 Experimental Objectives

The purpose of this study is to examine and compare the flow behavior and wall

convective heat transfer of swirl induced flow from both an axial and radial swirler at various Reynolds numbers. A separate study was also conducted on the combustor liner wall heat transfer on both the concave and convex walls of an annular combustor with a configuration of radial swirlers. As previously discussed, it is highly important with regards to the reliability and performance of gas turbine engine combustors to develop a full understanding of the wall heat transfer profiles in order to be able to design effective cooling schemes.

Since these experiments were not conducted under actual engine conditions, similarity analysis is required to relate the findings of this work to actual engine performance. To do this, two important parameters were investigated in this study. The first being the Reynolds number, which is defined as:

$$Re = \frac{inertial\ forces}{viscous\ forces} = \frac{\rho u D}{\mu} \tag{1.2}$$

where ρ is the fluid density, u is the mean flow velocity, D is the characteristic length, and μ is the (absolute) dynamic fluid viscosity. The second parameter investigated was the Nusselt number, which is defined as:

$$Nu = \frac{convective\ heat\ transfer}{conductive\ heat\ transfer} = \frac{hD}{k} \tag{1.3}$$

where h is the convective heat transfer coefficient, D is the characteristic length, and k is the thermal conductivity of the fluid. Heat transfer measurements were taken at multiple Reynolds numbers for each test setup to understand the effect of the swirlers at different engine operating conditions.

CHAPTER 2: EXPERIMENTAL SETUP

2.1 Can Combustor Experimental Setup

Figure 2.1 shows the experimental test rig used for heat transfer and PIV measurements. Air is supplied to the can combustor model from a pressure blower controlled by an adjustable frequency drive. This allows the blower to be manually controlled to achieve a desired flow rate and Reynolds number. Room temperature air was pulled through

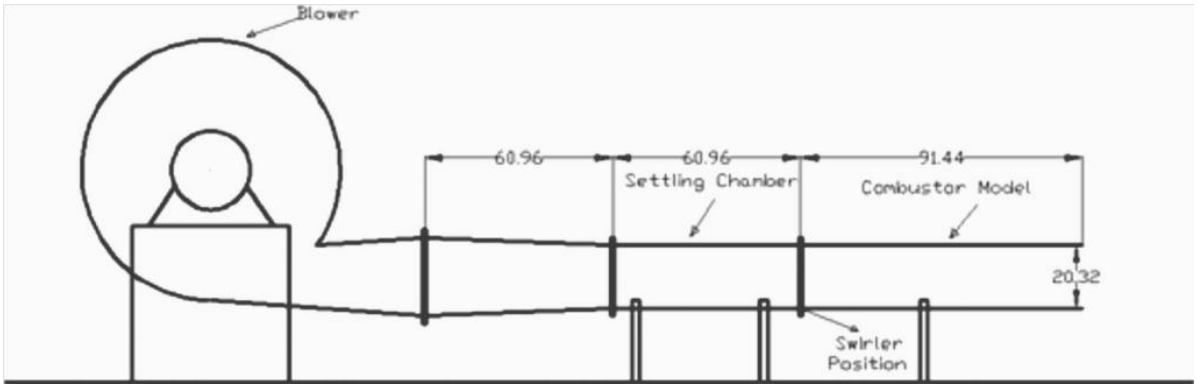

Figure 2.1. Experimental test setup (dimensions in centimeters)

the blower and passed through a 203-mm diameter settling chamber where the flow rate was monitored using a pitot probe. The air then exits the settling chamber through the swirler and into the can combustor model. For heat transfer measurements, a section of the combustor model was covered with surface heaters to provide a uniform heat flux along the wall.

2.1.1 Inlet Air Supply

A 3000 CFM pressure blower from New York Blower Company was used to provide the inlet air supply to the can combustor model. The blower was controlled by an Allen-Bradley PowerFlex 70 adjustable frequency AC drive. The dial pad control panel provided manual control of the blower frequency. For this study, the blower was set to speeds of 29Hz and 46Hz which provided Reynolds numbers of 50,000 and 80,000 respectively. Figure 2.2 shows an image of the blower setup.

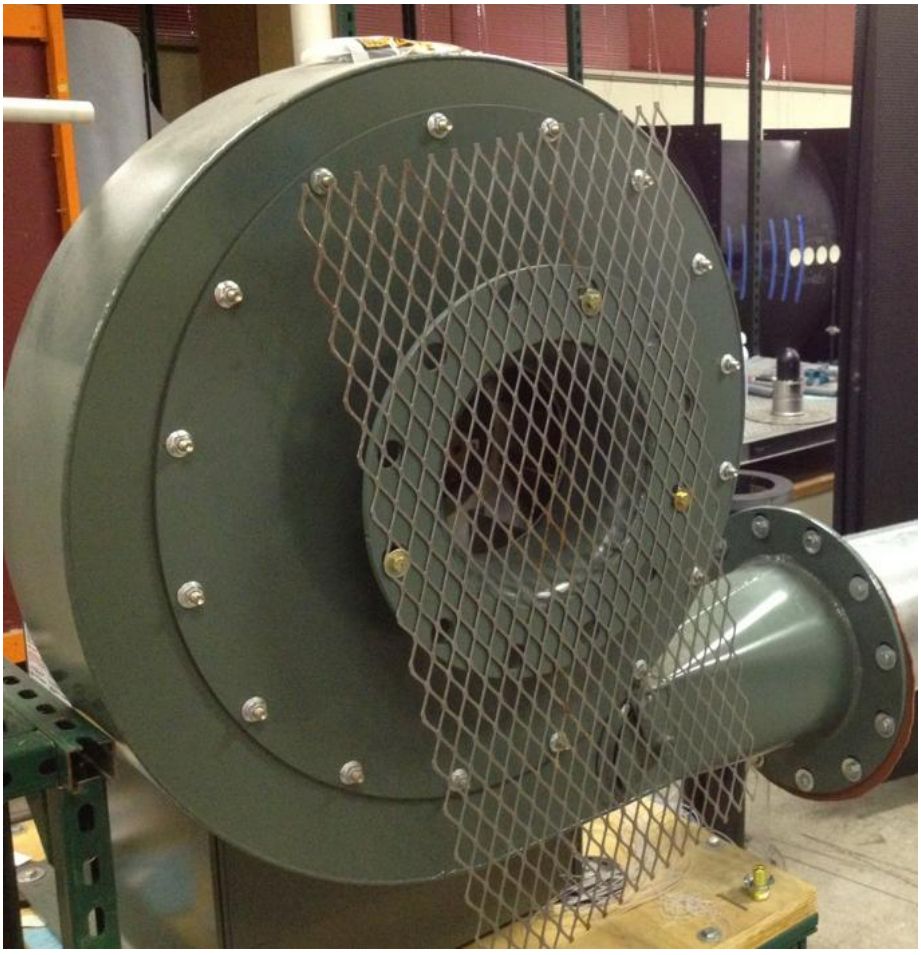

Figure 2.2. New York Blower Company 3000 CFM Pressure Blower inlet air supply (Photo by Author)

2.1.2 Swirler Design

The axial swirler design used for this study was provided by Solar Turbines and is shown in Figure 2.3.

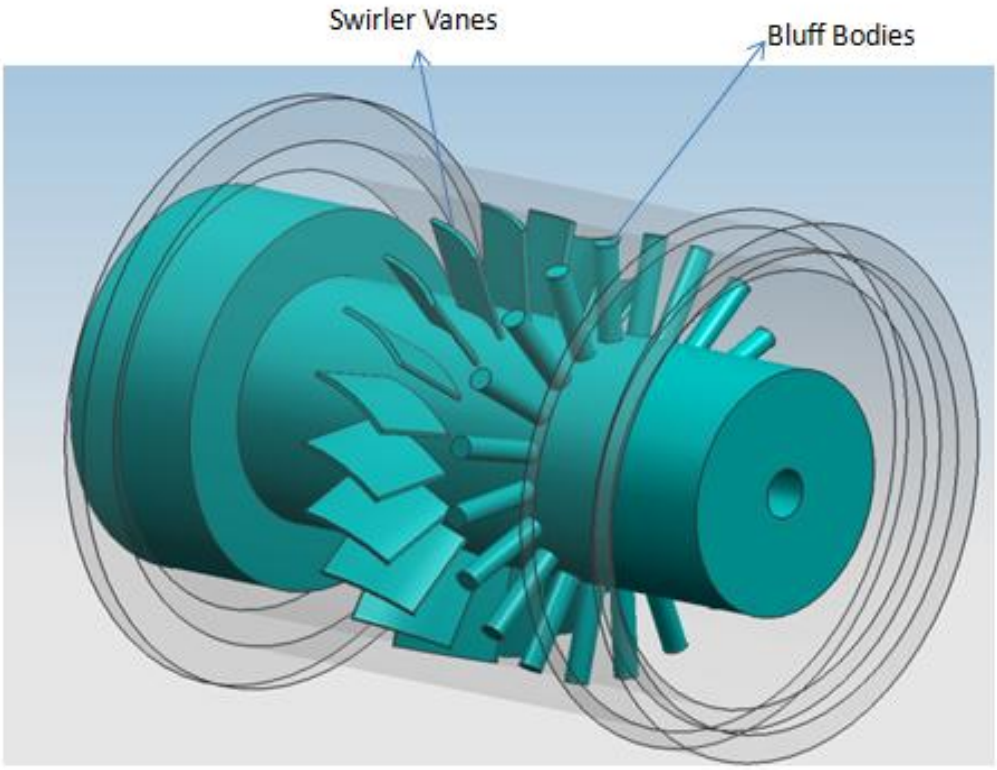

Figure 2.3. 3D CAD model of axial swirler

This design features a 20 vane configuration with a 45 degree swirl angle. The bluff bodies located immediately downstream of the vanes are fuel injectors which also provide flame stabilization in the actual combustor; however they are inactive for this study. The flow passes through this swirler encased between a central hub and the swirler walls with diameters of 44.45-mm and 79.25-mm respectively.

The radial swirler used in this study is shown in Figure 2.4.

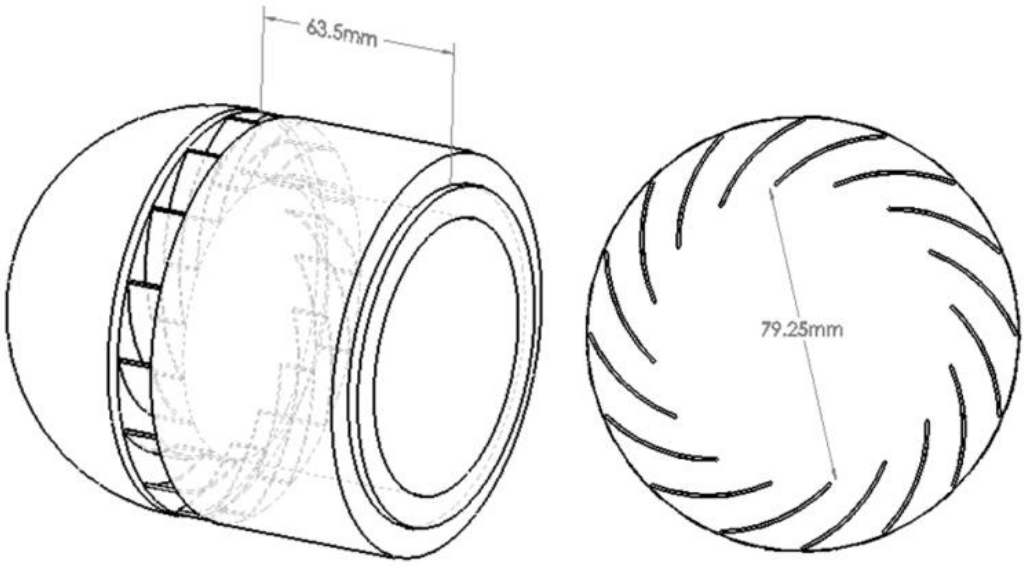

Figure 2.4. 3D CAD model of radial swirler (left) and vane configuration cross section (right)

This radial swirler contains 16 vanes and was designed to have the same intake area, swirl angle, and exit flow outer diameter as the axial swirler. With these parameters constant between the axial and radial swirlers, the Reynolds number of the flow through each swirler will be approximately the same and the comparison of the physics and flow behavior of each swirler can be more easily investigated. This swirler design also features an outlet throat that extends 63.5-mm downstream before the flow exits into the combustor model. The addition of the outlet throat was chosen based on the findings of King et al. [10] where it was concluded that an outlet throat allows for better air and fuel mixing prior to combustion, which therefore decreases the production of CO, UHC, and NOx. It is also important to note that the central hub that is found inside the axial swirler was not included in the radial swirler design. This was chosen from the recommendations

of King et al. [15] that it is important for radial swirlers to not have a central hub so the burnt combustion gasses can recirculate inside the swirler and provide flame stabilization.

2.1.3 Combustion Chamber

A 1:1 scale can combustor model was used for testing at cold flow conditions. The can combustor model used in this study was constructed out of an acrylic material to allow visibility for PIV measurements as well as minimal heat loss from the surface heaters to the wall. For heat transfer measurements, a section of the can combustor model was fitted with surface heaters to create a uniform heat flux at the wall. To observe the temperature distribution along the combustor wall, six evenly spaced viewport holes were cut from the wall opposite to the surface heaters for placement of an infrared (IR) camera. This combustor model can be seen in Figure 2.5. PIV measurements were conducted on a separate identical can combustor model without the viewport holes seen in Figure 2.6.

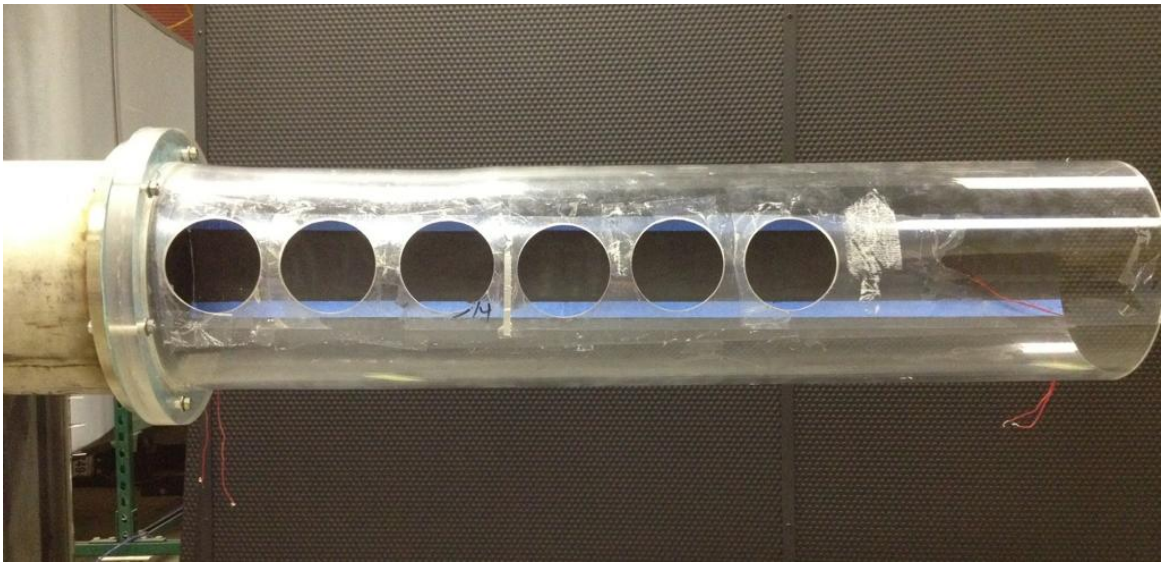

Figure 2.5. Can combustor model with viewports used for heat transfer measurements (Photo by Author)

Figure 2.6. Can combustor model used with PIV measurements (Photo by Author)

2.1.4 Surface Wall Heater

In order to provide a constant heat flux to the combustor model wall, the test section was fitted with two Minco© polyimide thermofoil surface heaters extending 762-mm axially along an approximate 70 degree section of the combustor wall. Each heater was connected to a variable output transformer which allowed for manual regulation of the temperature output of the heaters. The faces of the heaters were also covered with vertical strips of aluminum tape to help smooth the heat transfer profile and avoid visibility of the heating element profile while taking temperature measurements. For IR measurements, the accuracy of the camera is better when the emissivity of the surface is

close to that of a black body (emissivity equal to 1). To increase surface emissivity, the faces of the aluminum tape strips were painted flat black, which has an emissivity of approximately 0.95. The other sides of the heaters were attached to the combustor model with a thin layer of double sided tape. Figure 2.7 shows a diagram of the surface heater system.

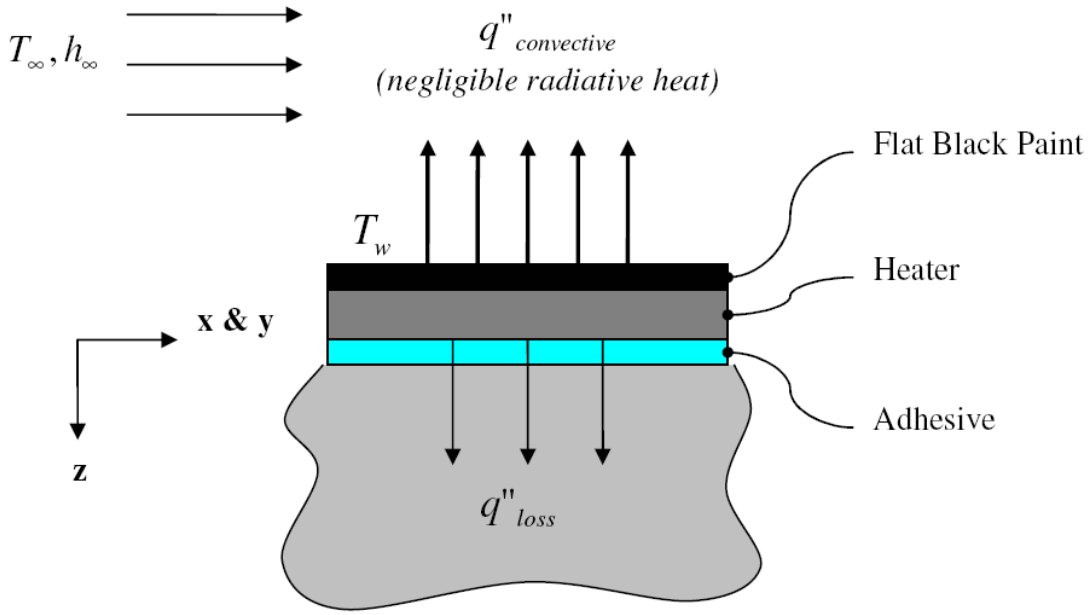

Figure 2.7. Diagram of surface heater system

An image of the actual test setup is shown in Figure 2.8. This image shows the view looking from the exit of the combustor into the test section towards the swirler. The heaters are attached to the combustor walls on the right-hand side of the image. The blue lines on the wall show the height of the viewing windows that were obtained by the IR camera. The viewport holes can be seen on the left-hand side of the image running parallel to the surface heaters.

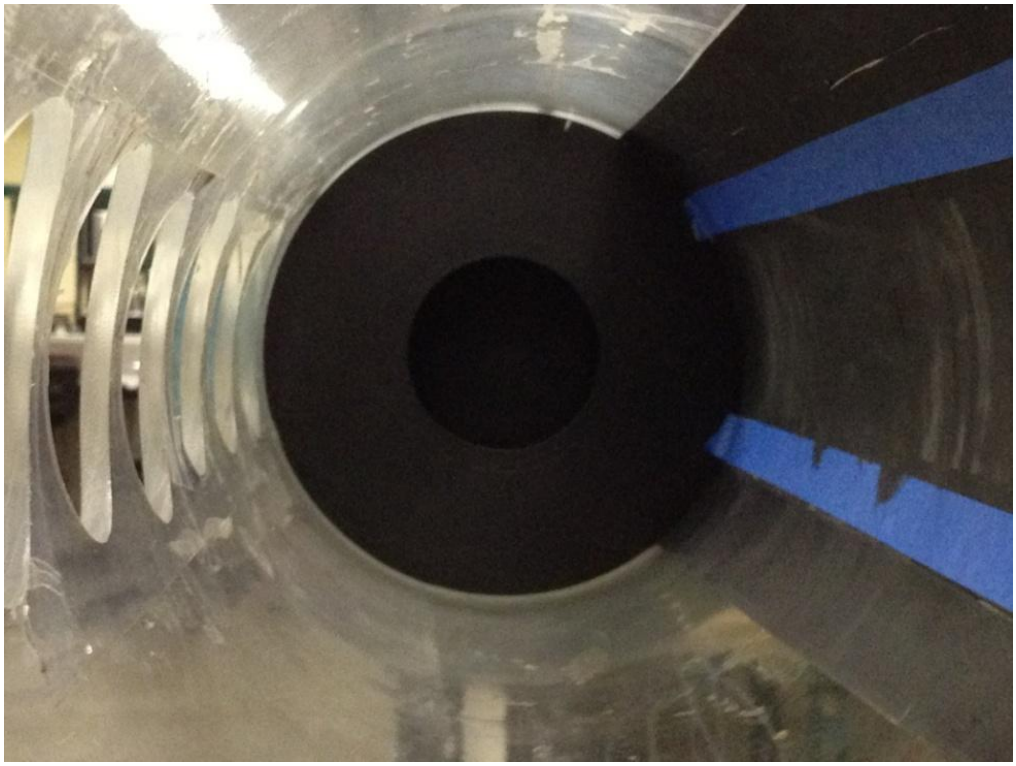

Figure 2.8. Can combustor surface heater setup (Photo by Author)

2.1.5 NANO-L-135-15 PIV Laser System

Seeding particles ranging in size from 0.25 to 60 microns were injected into the flow from a Rosco Model 1700 fog machine at the inlet of the blower. The air and seeding particle mixture passes through the settling chamber and swirler into the combustor model. A NANO-L-135-15 PIV laser system from Dantec Dynamics was used to create the laser sheet to illuminate the particles. The FlowSense 4M MkII camera with a 2048x2048 pixel resolution and refresh rate of 7.4Hz was set up perpendicular to the laser sheet to capture double frame images of the illuminated seeding particles inside the combustor. Measurements were taken at both the center axial plane and radial cross

sections of the flow. An adaptive correlation with interrogation area of 32x32 pixels was used to post process images in Dynamic Studio.

2.1.6 FLIR SC325 Infrared Thermal Imaging System

The FLIR SC325 was used to record temperature measurements on the combustor liner wall. The SC325 uses a focal plane array with an uncooled microbolometer for detection and has an image resolution of 320x240 pixels and a sensitivity of 0.5°C at 30°C. The SC325 can measure temperatures at a range of -20°C to 350°C at an image refresh frequency of 60 Hz. The camera was placed with the lens inside one viewport at a time and positioned to create a 101.6-mm wide viewing window. The other viewports were sealed while not in use. The camera was calibrated using a thermocouple placed on the face of one of the surface heaters. An image of the FLIR SC325 can be seen in Figure 2.9.

Figure 2.9. FLIR SC325 Infrared Thermal Imaging System

2.2 Annular Combustor Experimental Setup

The annular combustor test rig consists of a pressure blower controlled by an adjustable frequency controller at the inlet of the rig to provide airflow to a 2:1 scale quarter annulus combustor model. Room temperature air is pulled through the blower and sent to a settling chamber prior to entering the combustor model. The settling chamber and the combustor model each axially extend 914-mm and have identical geometry which can be seen in Figure 2.10. The radial swirlers used for this study are attached to a thin insert that fits between the settling chamber and combustor model. Surface heaters were attached to both concave and convex walls to provide a uniform heat flux for temperature and heat transfer measurements. Viewport holes were cut out from each side of the combustor model to view the surface heaters with an IR camera.

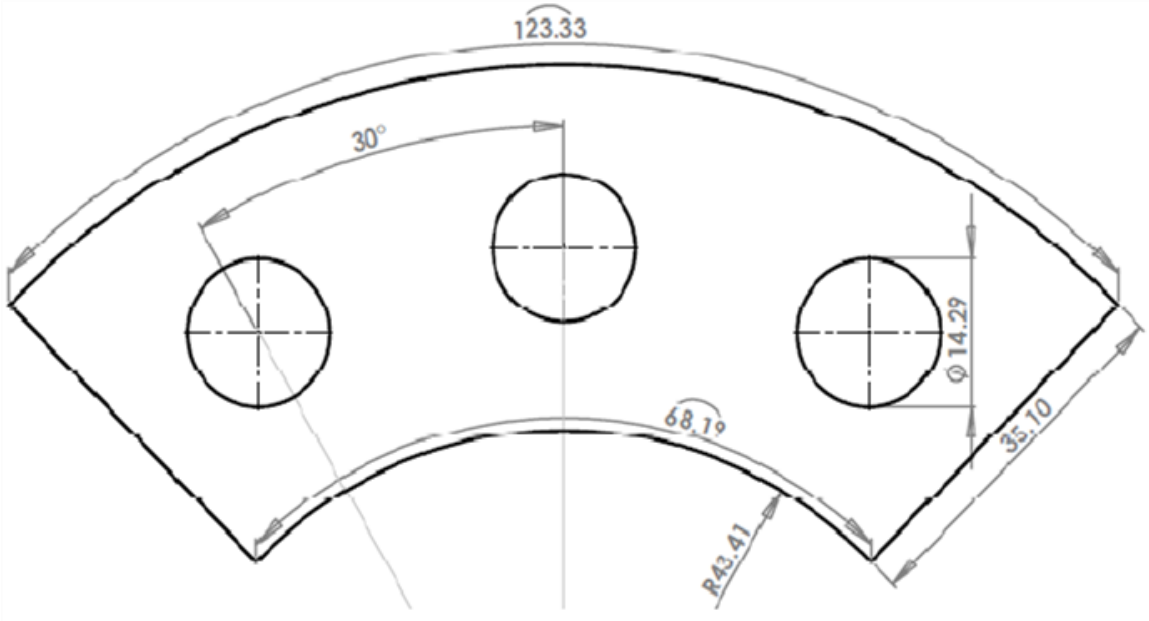

Figure 2.10. Quarter annulus test section dimensions (scale in cm)

2.2.1 Inlet Air Supply

A 9000 CFM pressure blower from Cincinnati Fans was used to provide the inlet air supply to the annular combustor model. The 15 Hp motor provides a maximum speed of 3525 RPM. The blower was controlled by a V-TAC 9 controller from Rockwell Automation. The dial pad control panel provided manual control of the blower frequency. For this study, the blower was set to speeds of 9.5Hz, 18.5Hz, and 34Hz which provided Reynolds numbers of 210000, 420000, and 840000 respectively. Figure 2.11 shows an image of the blower setup.

Figure 2.11. Cincinnati Fans 9000 CFM blower

2.2.2 Swirler

The radial swirler design used for this study was provided by Solar Turbines and is shown in Figure 2.12.

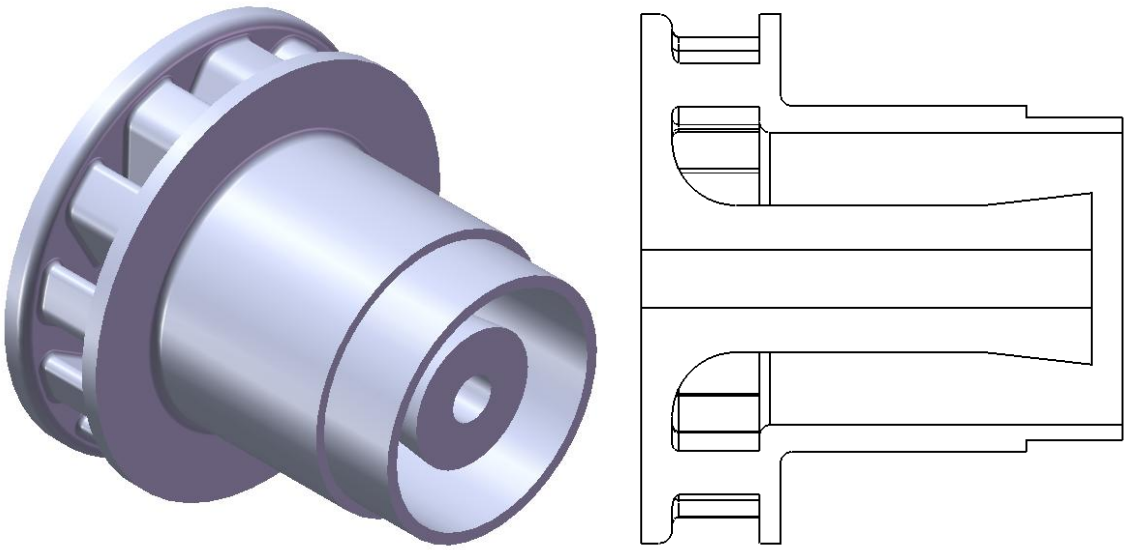

Figure 2.12. 3D CAD model of radial swirler (left) and flow path cross section (right)

This swirler is a 12 vane design that creates 12 constant area intake channels. In Figure 2.12, it is shown that air enters the swirler and passes through this swirler encased between a central hub and the swirler walls. Fuel is injected in this swirler through a central pilot location which is inactive for this study.

2.2.3 Combustion Chamber

The annular combustor model used in this study is a 2:1 scale quarter annulus test section with hydraulic diameter of 0.7-m constructed from sheet metal. The dimensions for the test section are given previously in Figure 2.10. Viewport holes were cut out of both the concave and convex sides of the test section for placement of an IR camera. Separate surface heater configurations were constructed for each concave and convex walls for heat transfer measurements. The concave and convex sides of the combustor model are shown in Figure 2.13 and Figure 2.14 respectively.

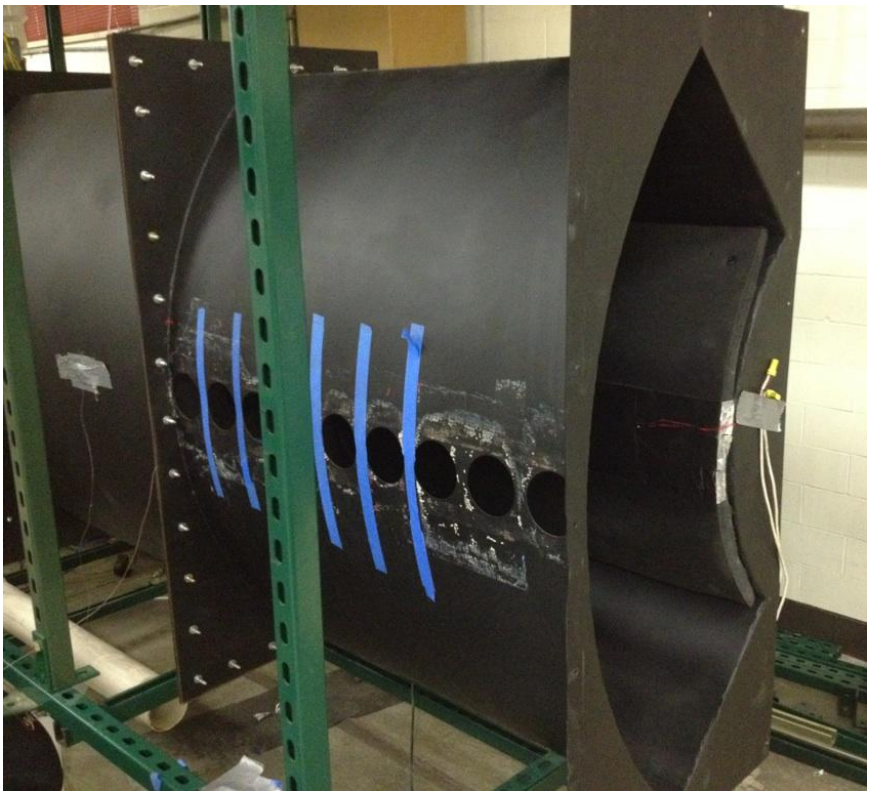

Figure 2.13. Concave side of annular combustor test section (Photo by Author)

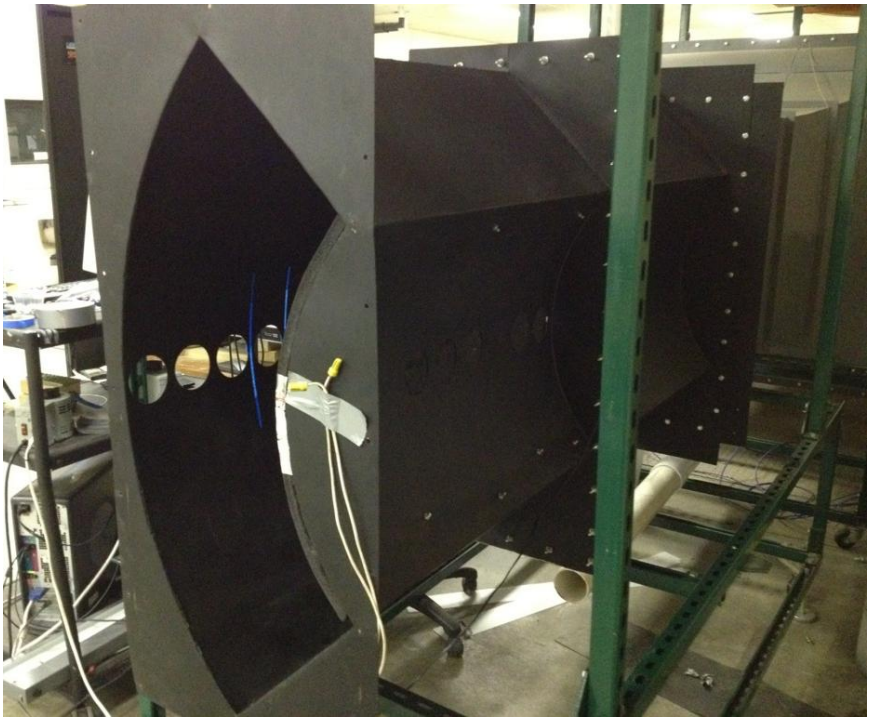

Figure 2.14. Convex side of annular combustor test section (Photo by Author)

2.2.4 Surface Wall Heater

For the concave wall temperature measurements, a single surface heater covered a 914-mm x 914-mm section of the wall. Using the same process seen in the diagram in Figure 2.7, the face of the heater to be viewed by the IR camera was painted flat black while the back of the heater was glued to a foam rubber pad. The rubber pad acts as a way to both secure the heater in place inside the test section as well as to insulate the heating system for minimal heat loss. The temperature output of the surface heater was manually controlled by a variable output transformer.

The convex wall setup consisted of the same two surface heaters used in the can combustor study. The surface heaters extended 762-mm axially along the convex wall of the annular combustor. The faces of the heaters to be viewed by the IR camera were again covered with vertical strips of aluminum tape to help smooth the heat transfer profile and avoid visibility of the heating element profile while taking temperature measurements**.** The back of the heaters were attached to a foam rubber pad with double sided tape. The foam rubber pad was then bolted into place inside the test section. An IR image of the convex wall heater setup is shown in Figure 2.15.

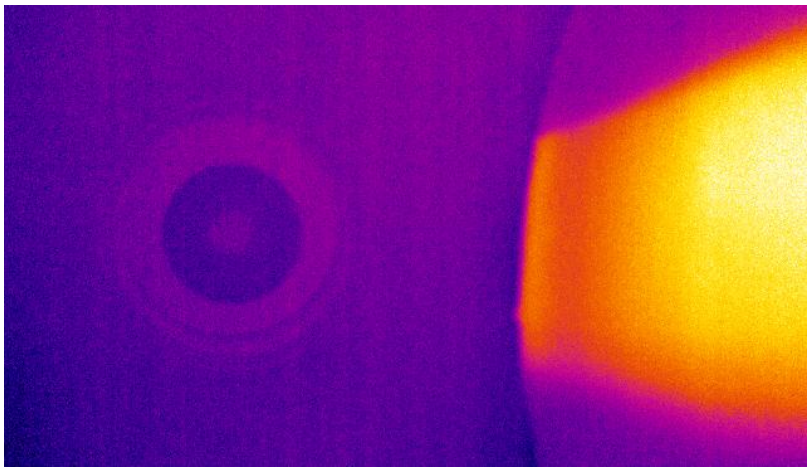

Figure 2.15. IR image of the convex wall surface heater setup (Photo by Author)

2.2.5 FLIR SC640 Infrared Thermal Imaging System

The FLIR SC640 was used to record temperature measurements on the annular combustor liner walls. The SC640 uses a focal plane array with a microbolometer for detection and has an image resolution of 640x480 pixels and a sensitivity of 0.1°C at 30°C. The SC640 can measure temperatures at a range of -40°C to 1,500°C at an image refresh frequency of 60 Hz. The lens of the camera was placed inside a single viewport hole to view the temperature on the opposite wall. The other viewports were sealed while not in use. The camera was calibrated using a thermocouple placed on the face of one of the surface heaters. An image of the FLIR SC640 can be seen in Figure 2.16.

Figure 2.16. FLIR SC640 Infrared Thermal Imaging System

2.3 Personal DAQ USB Data Acquisition Module

The OMB-DAQ-54 Personal Daq was used to process the thermocouple signals from the K and T type thermocouples used for this study. The OMB-DAQ-54 connects to a PC via a single USB cable that also acts as its power source. It has 10 single ended

channels which can also be used as 5 differential analog (up to ±20V full scale) or thermocouple input channels. The OMB-DAQ-54 also offers 16 programmable ranges and 500V optical isolation. An image of the OMB-DAQ-54 is shown in Figure 2.17.

Figure 2.17. The OMB-DAQ-54 Personal Daq

CHAPTER 3: EXPERIMENTAL METHODOLOGY

3.1 Flow-Field Measurement Methodology

Flow-field velocity distributions were measured experimentally using the method of Particle Image Velocimetry (PIV) for flow through each swirler at Reynolds numbers of 50,000 and 80,000. Measurements were taken along the center axial plane and radial cross sections of the combustor model. Figure 3.1 shows a diagram of the locations of these planes in the can combustor model.

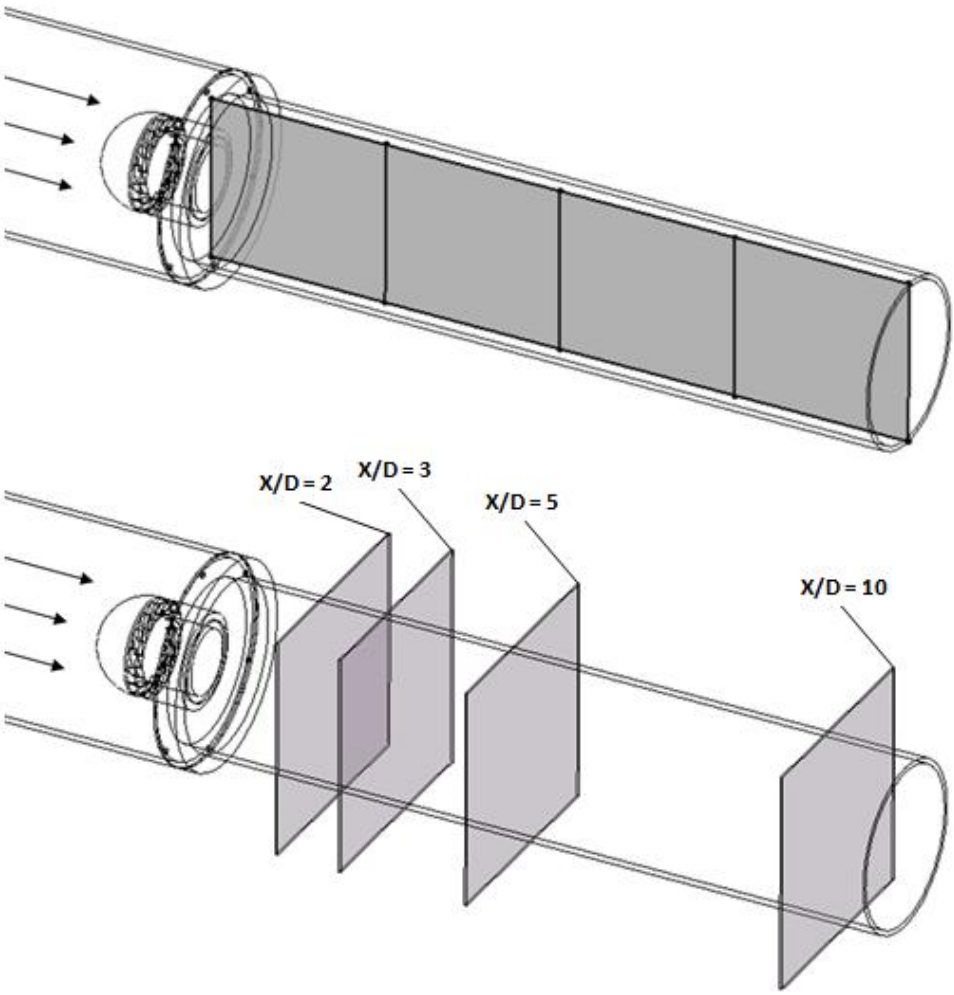

Figure 3.1. Diagram showing the locations of the center axial planes (top) and radial cross sectional planes (bottom) measured in PIV experiments

For measurements along the center axial plane, the NANO-L-135-15 PIV laser system was placed at the outlet of the combustor model, facing upstream, and produced a vertical laser sheet along the center line of the combustor. The FlowSense 4M MkII camera was aligned perpendicular to this laser sheet, facing into the side of the combustor, at four locations along the length of the combustor to capture the axial velocities of the flow. For measurements at the radial cross sections, the laser system was now aimed through the side of the combustor while the camera placed at the combustor outlet facing into the flow. In this configuration, the laser and the camera were both repositioned together to record measurements at four locations inside the combustor. The camera lens was placed 0.91m from the measurement plane for both setups and calibrated in Dynamic Studio using an image taken of a sheet of graph paper inserted into the measured plane.

3.1.1 Particle Image Velocimetry (PIV)

Particle Image Velocimetry (PIV) is a non-intrusive flow measurement technique that not only provides flow visualization, but is capable of accurately measuring entire flow field velocity distributions on both an average an instantaneous level. A PIV setup consists of a light source usually from a double pulse laser, a series of lenses to bend the light source to create a "light sheet" on the measured plane, seeding particles inside the measured flow, and a high speed camera to record images of the seeding particles as they are illuminated by the light sheet. A schematic of a standard PIV system can be seen in Figure 3.2.

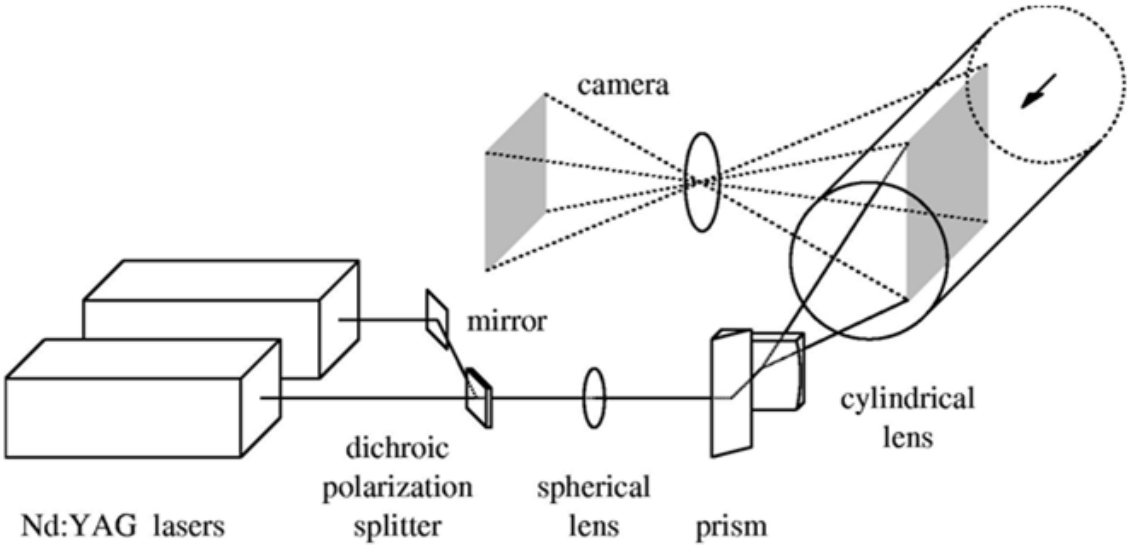

Figure 3.2. Schematic of a standard PIV setup [16]

In Figure 3.2, it is shown that two Nd:YAG lasers are used as the light source for this system. The reason for having two lasers is to be able to obtain very high rates of light pulses from the lasers. The lasers are pulsed to limit the exposure time of the seeding particles to the intense light in order to prevent oversaturation or streaking within the images. The lasers then are linked to the high speed camera through a synchronization module to allow the camera to record images at the exact time the laser pulsing occurs. The beam of light emitted by the lasers is passed through both a spherical and cylindrical lens. The spherical lens allows for regulation of the thickness of the beam while the cylindrical lens bends the light into what is seen as a light sheet. The light sheet is then aligned to be the plane of interest for flow measurement. As seeding particles are injected into the flow and pass through the light sheet, they are illuminated for the brief period that the laser is firing. The high speed camera is set up perpendicular to the light sheet in order to have complete focus along the length of the plane and to capture images of the

illuminated particles as they pass through the test section. As both lasers pulse sequentially, image pairs are produced that are later used for post processing and obtaining flow measurements. For this study, the NANO-L-135-15 PIV laser system was used and contained both lasers and lenses inside a single casing.

The images obtained from the high speed camera must be analyzed in order to obtain flow velocity measurements. This is done by dividing the images into a grid of small boxes of pixels known as interrogation areas. These interrogation areas are determined by the resolution of the images recorded by the camera and the particle size and density within the images. Typically, a higher resolution image will lead to the ability to use smaller interrogation areas which can ultimately provide better accuracy for flow measurements. Once the images are broken down into interrogation areas the image pairs are then compared and analyzed using a spatial correlation. A diagram of this process is shown in Figure 3.3.

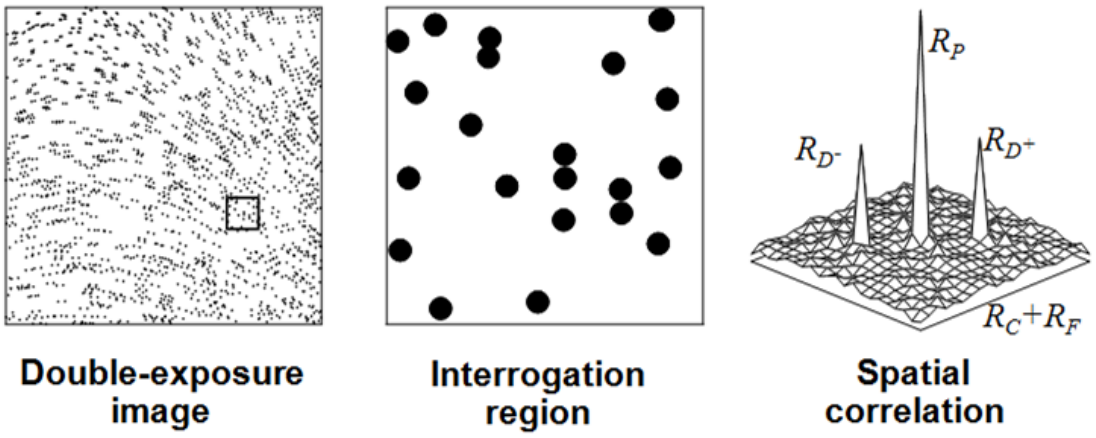

Figure 3.3. Diagram of PIV interrogation analysis [16]

The spatial correlation shown in Figure 3.3 is developed using the pixel intensity of the image pairs taken from the high speed camera. The spatial correlation is defined as

a relationship between the intensity and particle locations within the image. The relationship between in pixel intensity and particle locations used for this spatial correlation is shown in Equations 3.1 and 3.2 [17]:

$$\textbf{Spatial correlation}: \quad \boldsymbol{R(s) \cong \int I_1(X)\, I_2(X+s) dX} \tag{3.1}$$

$$\boldsymbol{Substitute}: \quad \boldsymbol{I = \langle I \rangle + I'} \tag{3.2}$$

where I_1 and I_2 are the intensities of the first and second images, X is the location of the pixel in the image, $\langle \boldsymbol{I} \rangle$ is the mean intensity of the image, and I' is the intensity fluctuation.

To perform the spatial correlation analysis, interrogation areas are observed one at a time. The spatial correlation is applied to each pixel within the interrogation area. While each of the particles in the image pairs originally has an equal probability of being a match, there can only be one true pair. With correctly sized interrogation areas, the variations between the motion of each particle can be minimized. As the spatial correlation is applied to each pixel within the interrogation area, similar motion patterns will begin to develop for all the particles. Since the particle motion fluctuation should be low, the analysis will be able to narrow down each possible displacement to an approximately consistent trajectory for each particle in the interrogation area and correctly match the particles in the image pairs. The spatial correlation analysis process can be seen in Figure 3.4.

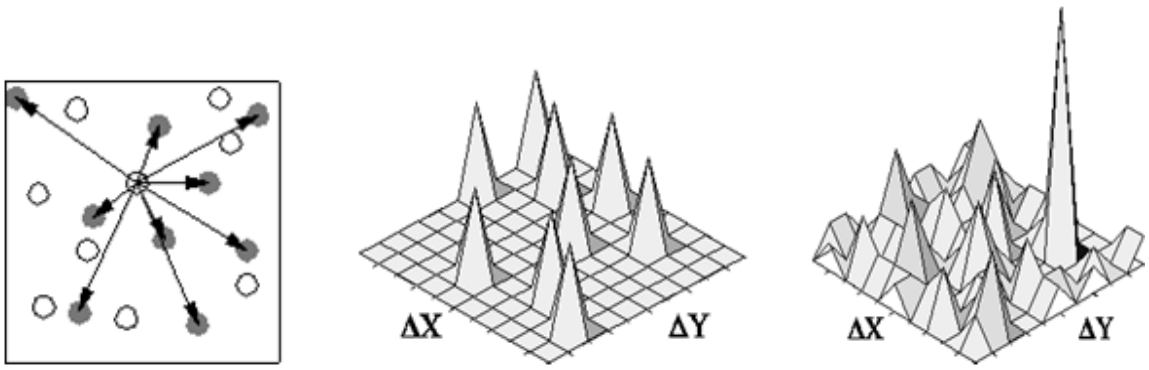

Figure 3.4. Spatial correlation analysis [16]

In Figure 3.4, the far left image shows an overlay of a set of image pairs with the particles of the first and second images being represented by the empty and shaded circles respectively. The array of arrows stemming from the central empty circle displays all the possible trajectory combinations for this particle. This center image shown in Figure 3.4 shows the initial application of the spatial correlation for this particular particle. The set of peaks seen in this image represents the equal probability that particle has to be matched with the other shaded particles. The image on the far right of Figure 3.4 shows the final result of the correlation once every pixel in the interrogation area has been analyzed and compared with each other. The large peak shown in this image displays the highly probably X and Y direction displacement of the particle. The X and Y displacements are converted to actual lengths through calibration of the system where the amount of pixels per unit length is determined. Since the time between images is manually set, the displacement of the particles can be converted into a velocity. This analysis is then conducted over every interrogation region in the image pairs to construct a map of the flow field.

3.1.2 PIV System Settings

In order to obtain images with a measureable number of particles the settings of the laser power, time between laser pulses, fog machine power, the time the fog machine power was turned on to inject seeding particles, and the time period between switching the fog machine off and starting data collection were varied. The laser power setting controls the intensity of the light sheet, which impacts how brightly the seeding particles in the flow will be illuminated. The time between pulses controls the time between image pairs and is regulated to minimize seeding particles exiting the interrogation area between an image pair. The fog machine power and the time the fog machine was turned on both regulate the amount of fog particles injected into the system. At higher flow rates, more seeding particles are needed since they exit the test section at a faster rate. The last setting varied was the time between switching the fog machine off and starting data collection. It was necessary to stop injecting seeding particles for a time period prior to taking measurements since continuous running oversaturated the test section with seeding particles due to the high level of recirculation in the test section. At each measurement location, roughly 50-100 images were recorded and time averaged to capture the flow behavior. The settings used in this study are shown for a 32x32 pixel interrogation area and were developed based on the results from multiple test runs until a measurable distribution of particles was attained.

	Reynolds Number	
Settings	**50,000**	**80,000**
Laser Power	10	10
Time Between Pulses	25μs	15-25μs
Fog Power	4	8
Fog Time On	5s	10s
Time Between Acquisition and Fog Injection	5s	5s

3.2 Steady State Heat Transfer Methodology

For experiments on both the can and annular combustors, the blower was set to different frequencies to produce certain Reynolds numbers. Dynamic pressure readings were taken in the settling chambers of each rig and converted to velocities to obtain the correct blower settings to produce the required Reynolds numbers. The surface heaters for each experiment were activated for each blower setting and left alone for approximately one hour to reach steady state wall temperatures. An IR camera was placed in the viewport holes on the side opposite the surface heaters to view the heated walls. An image of the setup used for the can combustor study was shown previously in Figure 2.8. A CAD model of the annular rig heat transfer setup is shown in 3.5.

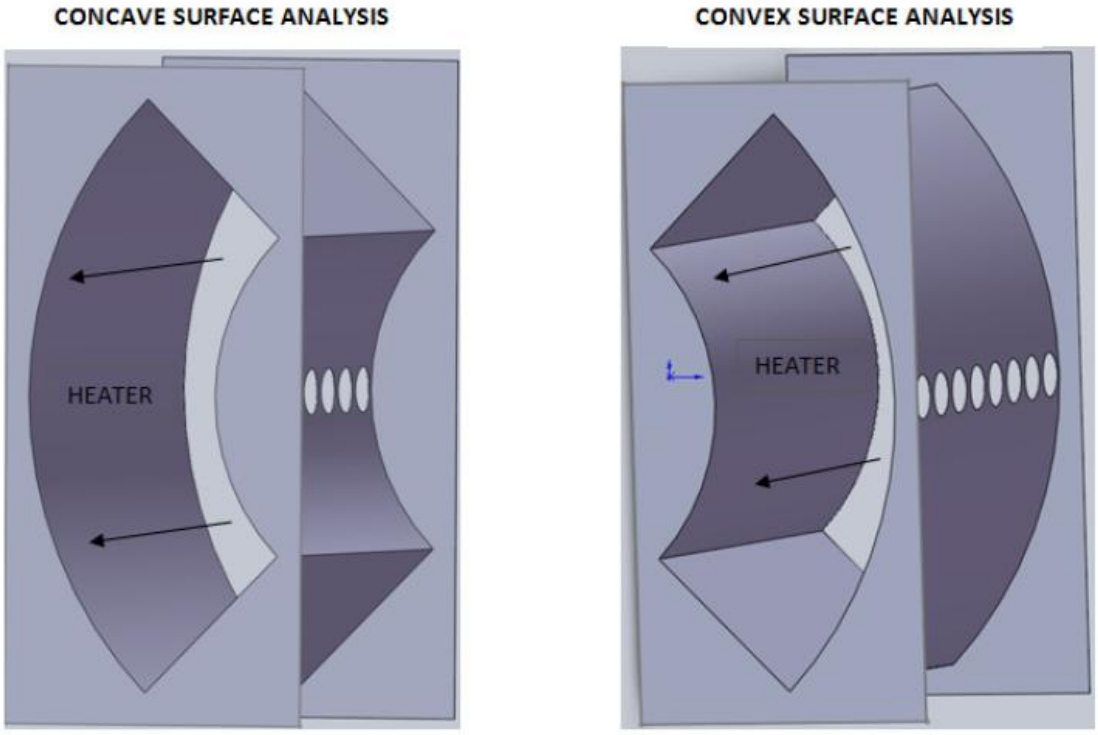

Figure 3.5. Annular combustor heat transfer diagram [4]

Steady state combustor wall heat transfer measurements were obtained using the basic convective heat transfer equation,

$$h = \frac{Q - Q_{loss}}{A(T_{wall} - T_{air})} \tag{3.3}$$

where h is the convective heat transfer coefficient, Q is the constant heat flux applied by the heater, Q_{loss} is the estimated conduction heat loss, A is the surface area of the heater, T_{wall} is the measured wall temperature from the FLIR SC325 and FLIR SC640 for the can combustor and annular combustor experiments respectively, and T_{air} is the air temperature recorded from a K-type thermocouple using the OMB-DAQ-54 Personal Daq USB Data Acquisition Module. The heat input value was calculated using the voltage setting on the variable output transformer and the resistance rating of the surface heater.

$$Q = \frac{V^2}{R} \tag{3.4}$$

Heat loss was estimated to be 5% based on the calibration curves developed on the same can and annular combustor setups in the studies by Abraham [3] and Sedalor [4]. These plots are shown in Figure 3.6.

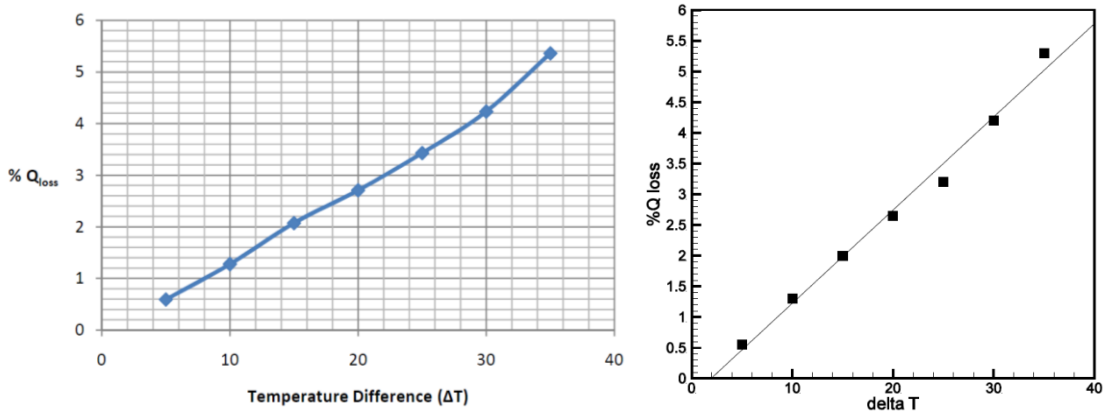

Figure 3.6. Measured heat loss profiles obtained from the studies of Abraham [3] (left) and Sedalor [4] (right). Abraham, S., 2008, "Heat Transfer and Flow Measurements on a One-scale Gas Turbine Can Combustor Model," MS thesis, Department of Mechanical Engineering, Virginia Polytechnic Institute and State University, Virginia. Sedalor, T., 2009, "Heat Transfer and Flow Characteristics in a Low Emission Annular Combustor," MS thesis, Department of Mechanical Engineering, Virginia Polytechnic Institute and State University, Virginia. Used under fair use, 2012

3.2.1 Similarity Analysis

In order to compare these experimental results to actual engine performance, similarity analysis must be done. Actual engine conditions can be approximated with an air temperature of 1850K, k_{air} at 1850K of 0.124 W/m·K, and an operating pressure of 20atm. The test conditions for both the can and annular combustor models consist of an air temperature of 293K, k_{air} at 293K of 0.0263 W/m·K, and an operating pressure of 1atm. Similarity analysis shows that:

$$(NU)_{actual} = (NU)_{test}$$

$$\left(\frac{hD}{k}\right)_{actual} = \left(\frac{hD}{k}\right)_{test}$$

Therefore,

Can Combustor Experiments

$$h_{actual} = \left(\frac{k_{actual}}{k_{test}}\right)\left(\frac{D_{test}}{D_{actual}}\right)h_{test} = 4.71 \times 1 \times h_{test} = 4.71h_{test}$$

Annular Combustor Experiments

$$h_{actual} = \left(\frac{k_{actual}}{k_{test}}\right)\left(\frac{D_{test}}{D_{actual}}\right)h_{test} = 4.71 \times 2 \times h_{test} = 9.42h_{test}$$

From similarity analysis, the heat transfer results produced in the can combustor study will be 4.71 times lower than actual engine conditions, while the annular combustor experiment heat transfer results will be 9.42 times lower than actual engine conditions.

CHAPTER 4: RESULTS

4.1 Can Combustor Flow Path and Heat Transfer Results

4.1.1 Flow-Field Visualization and Behavior

Radial cross section velocity profiles are shown at various lengths along the combustor with respect to the swirler diameter in Figures 4.1 and 4.2. For both Reynolds numbers tested, the radial swirler produced significantly larger radial velocities than the axial swirler. Since the radial swirler inducts air purely tangentially, flow entering the radial swirler contains only a radial component of velocity. This differs from the axial swirler where air enters purely axially and the passage of the vanes introduces the radial velocity component. Radial velocities from the axial swirler were also found to show a much more uniform distribution than those from the radial swirler.

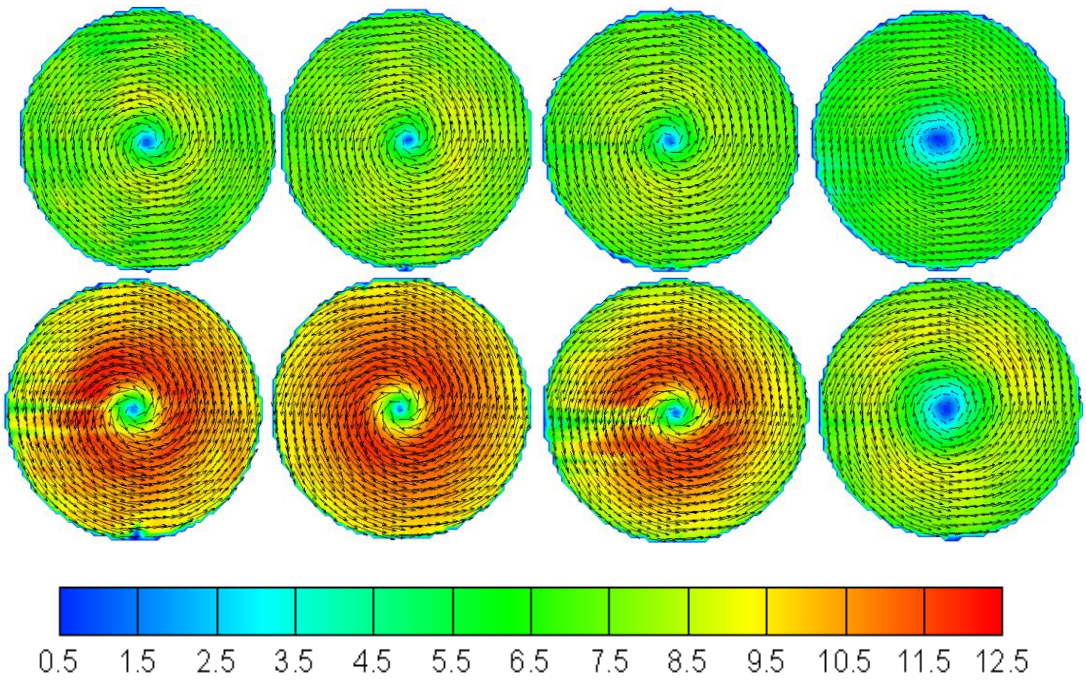

Figure 4.1. Radial velocity distributions produced by the axial swirler (top row) and the radial swirler (bottom row) at radial cross-sectional planes at X/D locations of 2 (far left), 3 (middle left), 5 (middle right), and 10 (far right) at Re = 50,000. (scale in m/s)

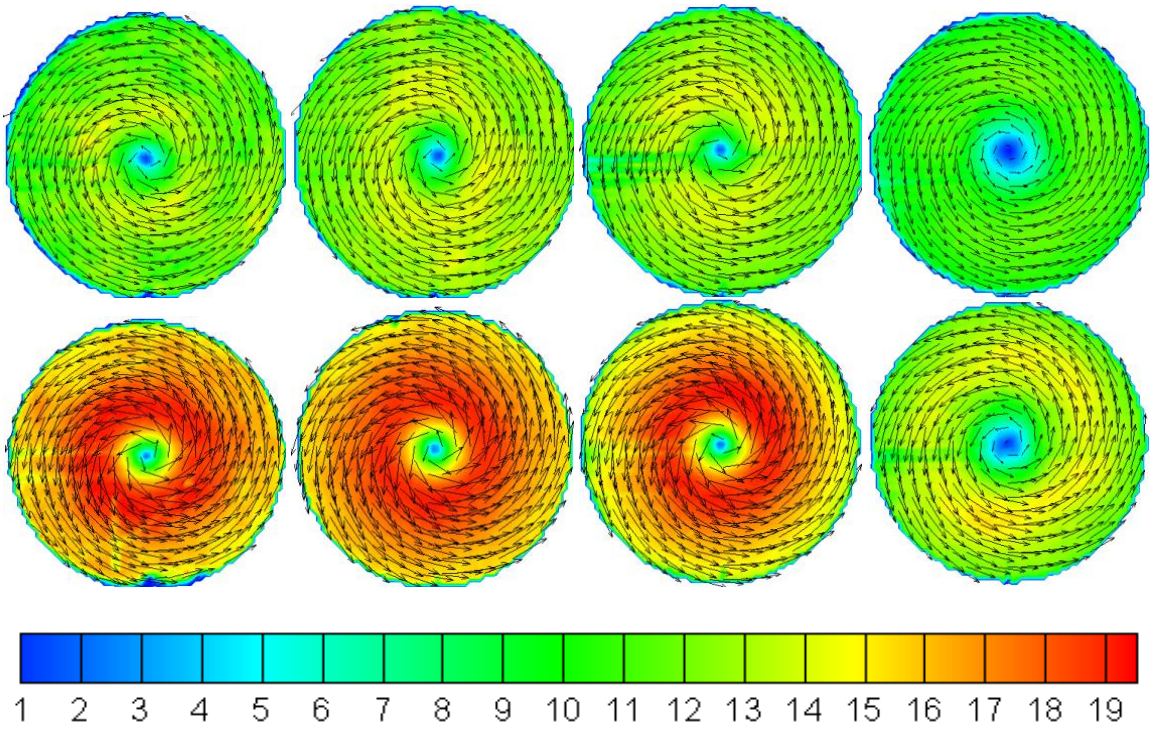

Figure 4.2. Radial velocity distributions produced by the axial swirler (top row) and the radial swirler (bottom row) at radial cross-sectional planes at X/D locations of 2 (far left), 3 (middle left), 5 (middle right), and 10 (far right) at Re = 80,000. (scale in m/s)

It is also shown in Figures 4.1 and 4.2 that each flow revolves around a low velocity core. The physics of these cores are critical to the performance and effectiveness of the swirlers and are discussed later in detail. As the flow progresses through the combustor, both swirlers produce little swirl decay until it nears the exit of the combustor model where the flow is exhausted into atmospheric conditions. This decay can be seen in Figures 4.1 and 4.2, as the velocity profiles of the outer rotating section of the flow and the core flow remain approximately constant until the exit location.

Velocity profiles along the center axial plane of the combustor are shown in Figures 4.3 and 4.4. It is important to note that due to images having been recorded through the curved surface of the combustor model made from an acrylic material,

measurements have been slightly distorted due to refraction. Corrections to these measurements are currently being investigated. Despite this distortion, the current data provides a sufficient understanding of the flow behavior inside the combustor model. Flow enters and accelerates through the swirler where it begins to rotate as it passes over the vanes. Due to this rotation, the flow exits each swirler and radially expands outwards until impinging on the combustor wall. The rotation induced by the swirler causes a low pressure core to form inside the flow. In many cases, the degree of rotation is so large that the pressure inside the core becomes low enough to cause the core flow to move in the upstream direction while the outer rotating section of the flow progresses downstream. This reverse flow effect causes the core section of the flow to become a major recirculation zone and creates smaller recirculation zones between the core and the outer flow. This is a desired effect, as it promotes mixing of the burnt combustion gases and assists in establishing a more uniform temperature distribution throughout the combustor. In Figures 4.3 and 4.4, the effect can be seen for both the axial and radial swirlers. For both Reynolds numbers, the radial swirler produced a higher degree of rotation which resulted in a thicker and larger velocity core flow when compared to the axial swirler. The thicker core also restricts the exit area from the radial swirler into the combustor which causes the flow to accelerate and results in overall higher axial velocities.

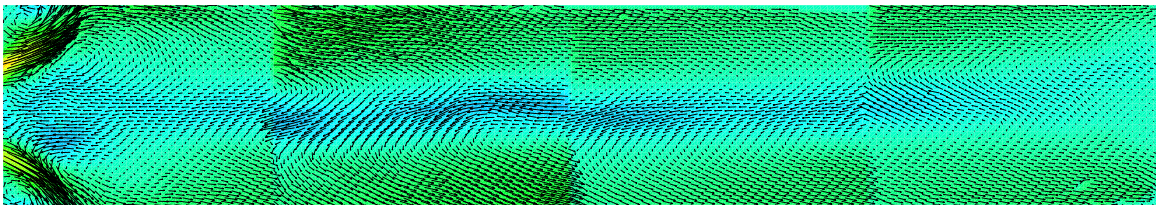

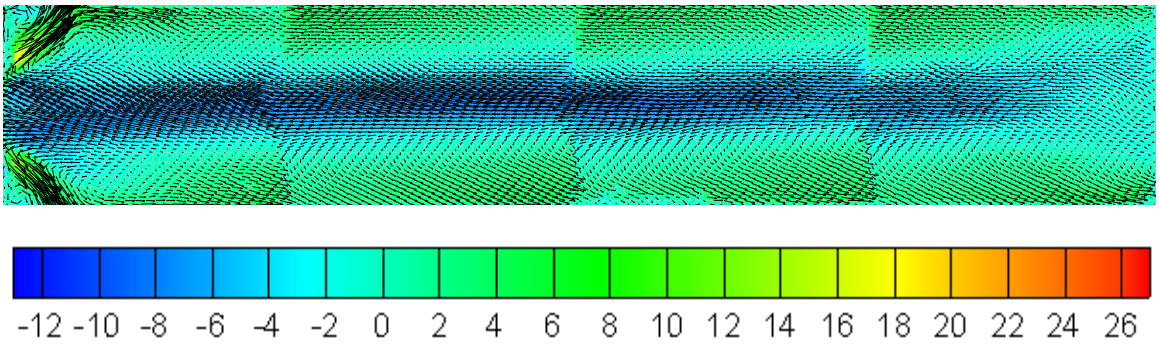

Figure 4.3. Axial velocity distributions produced by the axial swirler (top) and the radial swirler (bottom) along the center axial plane of the combustor at Re = 50,000. (scale in m/s)

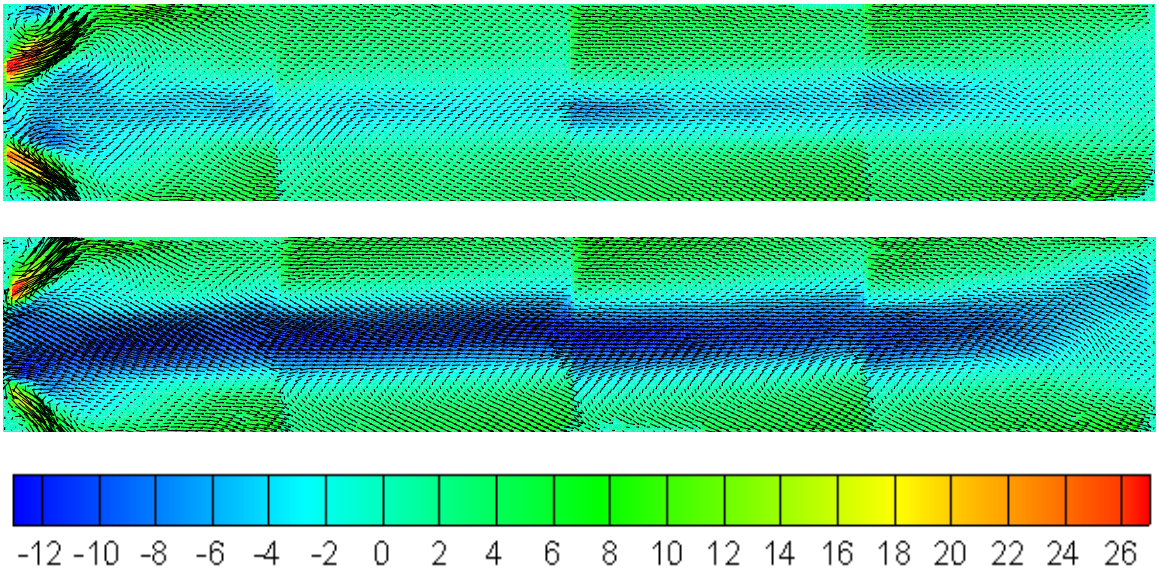

Figure 4.4. Axial velocity distributions produced by the axial swirler (top) and the radial swirler (bottom) along the center axial plane of the combustor at Re = 80,000. (scale in m/s)

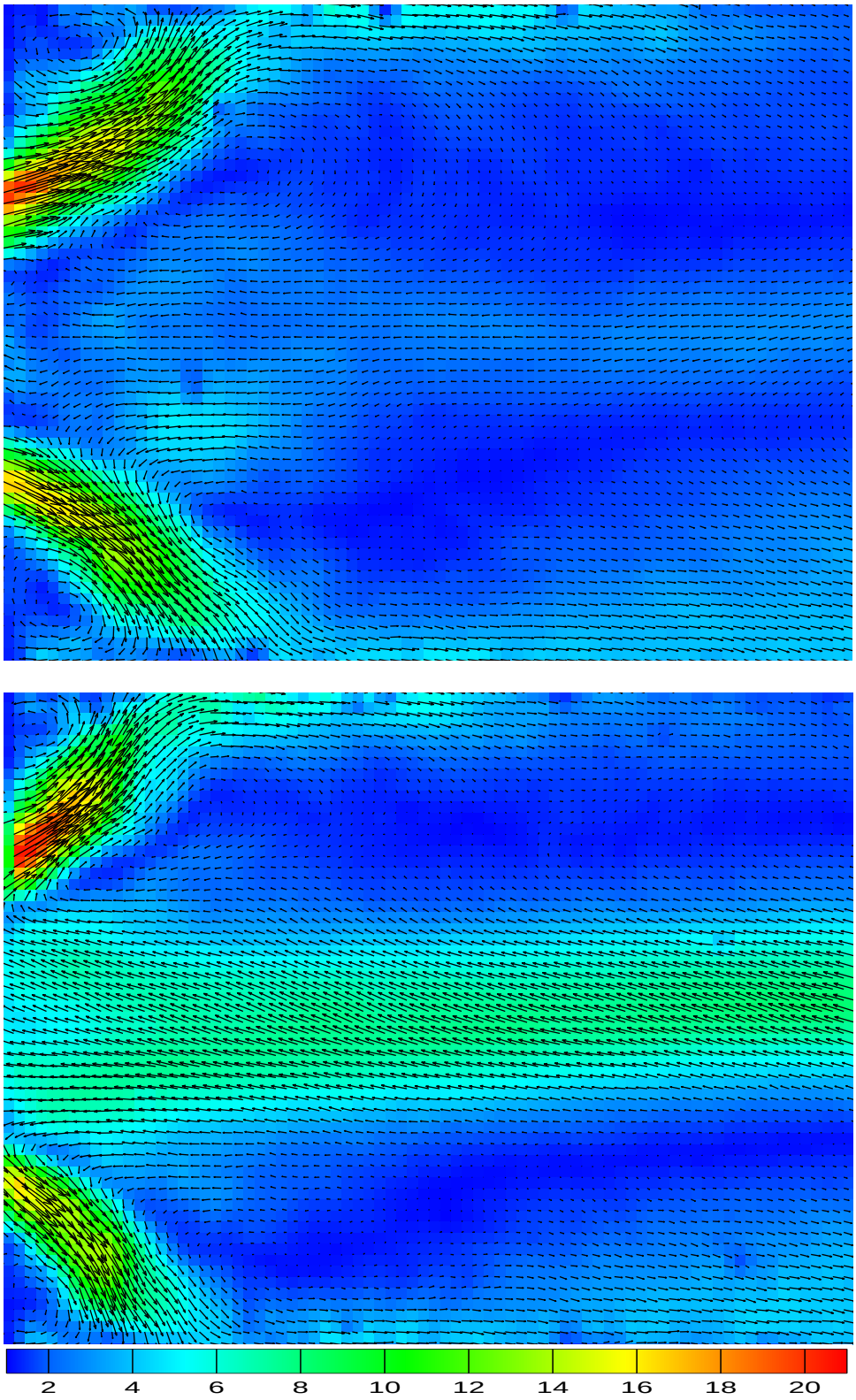

Figure 4.5. Combustor entrance total velocity comparison between the axial swirler (left) and the radial swirler (right) at Re = 50,000. (scale in m/s)

An enlarged swirler exit profile for both axial and radial swirlers at a Reynolds number of 50,000 is shown in Figure 4.5. In both images, the flow exits the swirler at approximately the same angle into the combustor. The axial swirler exit shows a longer and thicker entrance section at mid range velocities due to the less restricted expansion from the smaller reverse core flow. It is also seen that the flow from the core does not enter back into the axial. This is prevented with the design of the axial swirler containing a central hub. Since the radial swirler does not contain this hub in its design, the reverse core flow is allowed to continue back into the swirler where a small recirculation zone will be established at the back wall of the swirler. This flow characteristic is used in industry as a flame holding technique for radial swirlers and is not needed for designs such as the axial swirler where flame holding is achieved behind the bluff body fuel injectors. The remaining section of the core is mixed into the mainstream flow with the new incoming air over the swirler vanes. Figure 4.5 also shows the recirculation zones established at the entrance of the combustor. In each image there are two main recirculation zones, excluding the core. The zones are located between the entrance stream from the swirler and the core flow, as well as behind the entrance stream along the back wall. The axial swirler is capable of producing larger recirculation zones in these areas. This is a result of the less restricted exit from the axial swirler by the reverse core flow. This behaves as expected. Since the combustor entrance velocities from the radial swirler are higher than those produced by the axial swirler, less of this entrance flow is broken off to recirculate at the back wall. The thicker core of the radial swirler also provides less available area between the core and outer flow to establish a recirculation zone.

4.1.2 Steady State Heat Transfer Coefficient Distribution

Heat transfer coefficient distributions along the combustor wall for flow through both swirlers at Reynolds numbers of 50,000 and 80,000 are shown in Figures 4.6 and 4.7 respectively. The Nusselt number along the centerline of the heated area was also computed and shown in Figure 4.8.

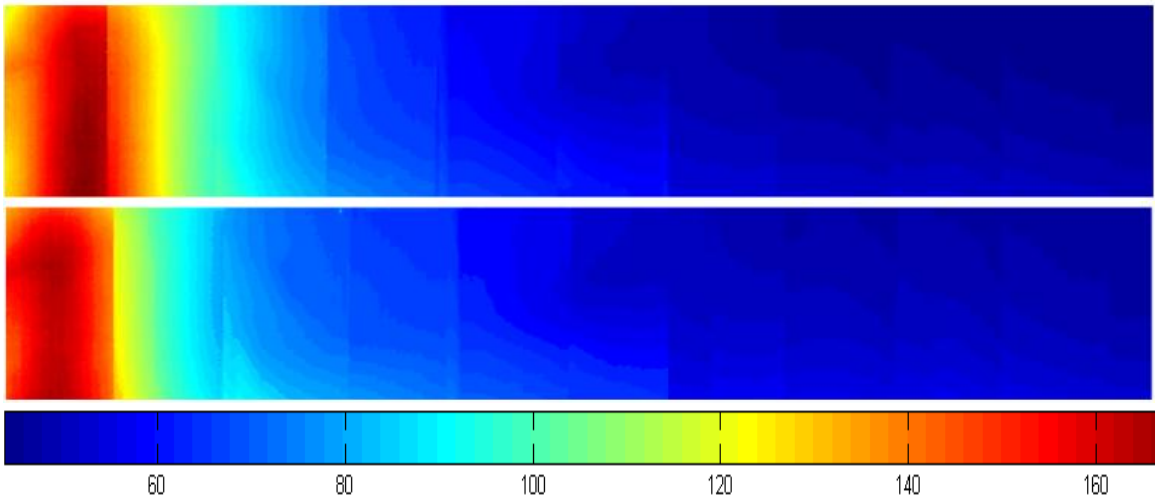

Figure 4.6. Heat transfer distribution for flow at Re=50,000 through the axial (top) and radial (bottom) swirlers with flow direction from left to right (scale in W/m^2K)

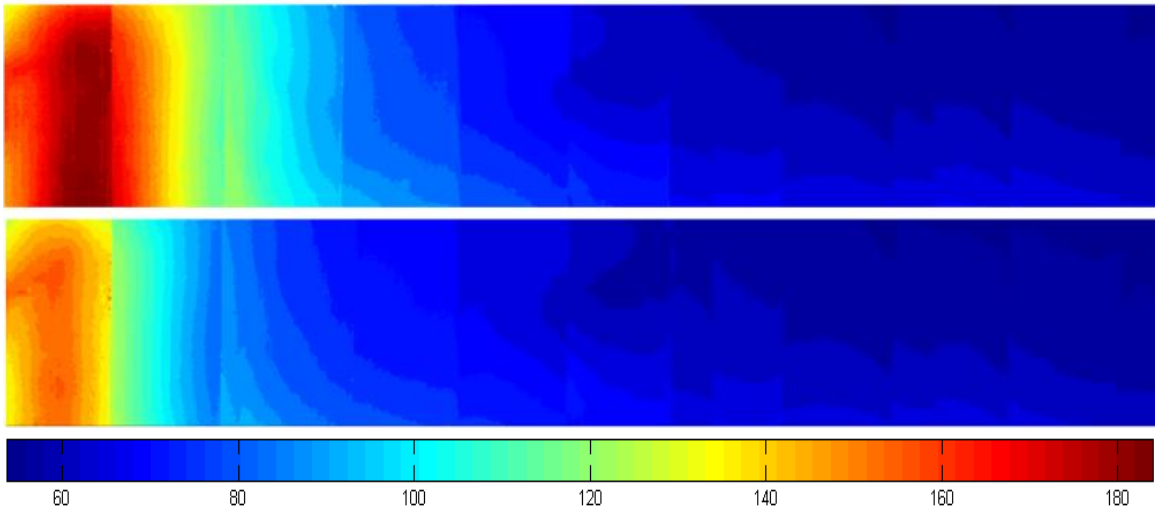

Figure 4.7. Heat transfer distribution for flow at Re=80,000 through the axial (top) and radial (bottom) swirlers with flow direction from left to right(scale in W/m^2K)

Images from the six viewport holes were stitched together to form these profiles. Peak heat transfer locations for each case correspond to the position where the flow exits the swirlers and impinges on the combustor wall. The magnitude of the heat transfer begins to decay after this location. Figures 4.6 and 4.7 show that flow through the axial swirler produces a wider area of high heat transfer. This is due to the larger recirculation zones in front and behind the flow entering the combustor through the axial swirler, as shown in the PIV results in Figure 4.3. It can be seen in both Figures 4.6 and 4.7 that the heat transfer coefficient produced by the radial swirler decays more rapidly than the profiles shown by the axial swirler. This decay is attributed to the larger reverse core flow as well as the higher radial velocities that are produced by the radial swirler. The enhanced mixing that results from both of these characteristics causes the flow to reach a steady temperature sooner than the flow from the axial swirler. This is also the reason why the flow from the radial swirler has a lower maximum heat transfer coefficient value. Typically, a higher flow velocity near the wall would result in a higher heat transfer coefficient. Although the radial swirler produces higher radial velocities, the higher maximum heat transfer coefficient is seen with the axial swirler. The large amount of reverse flow in the core of the radial swirler flow extracts a greater amount of the warm air exiting the combustor. This air is carried back inside the swirler where it mixes with the mainstream flow exiting the swirler vanes. These two flows mix together inside the swirler throat and enter the combustor at a higher temperature than the axial swirler flow. This higher temperature prevents the radial swirler flow from producing a larger maximum heat transfer coefficient.

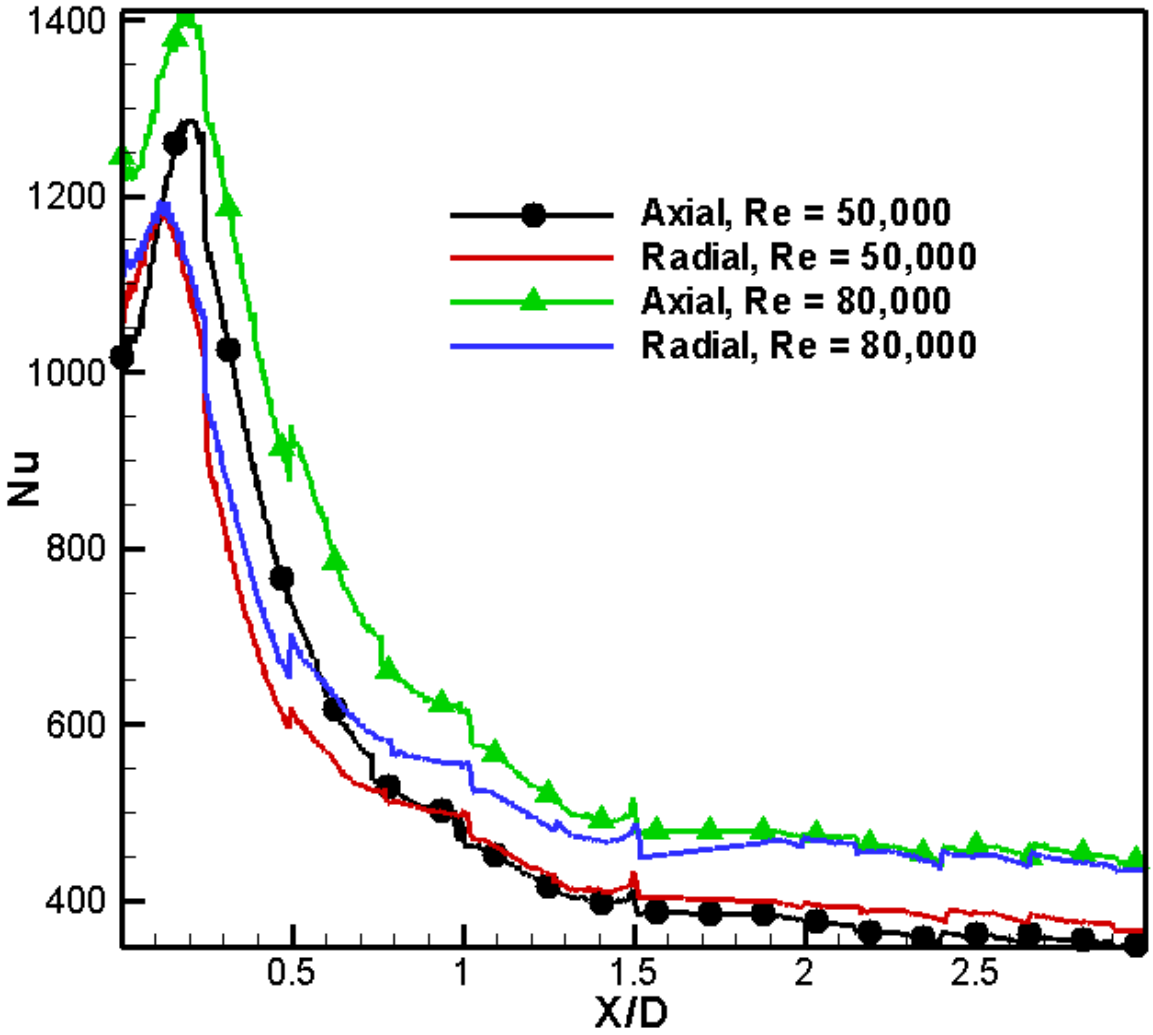

Figure 4.8. Nusselt number distribution along combustor wall with reference to combustor diameter for axial and radial swirlers at Re=50,000 and Re=80,000

4.2 Annular Combustor Heat Transfer Results

Heat transfer coefficient distributions along the annular combustor concave and convex walls at Reynolds numbers of 210000, 420000, and 840000 are shown in Figures 4.9, 4.10, and 4.11 respectively.

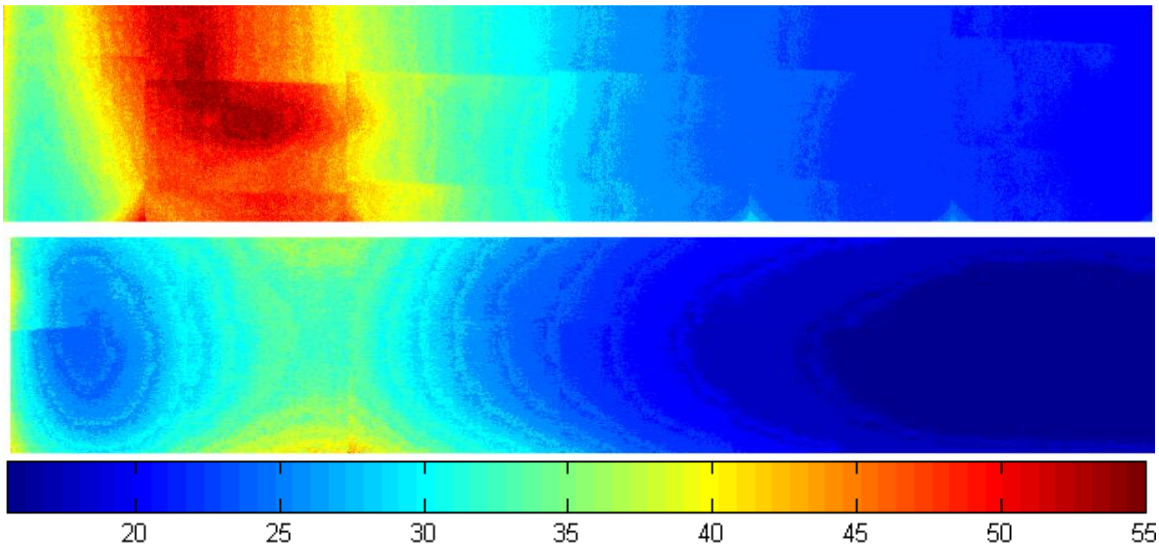

Figure 4.9. Heat transfer coefficient distribution along the concave (top) and convex (bottom) walls for Re = 210,000 with flow direction from left to right (scale in W/m^2K)

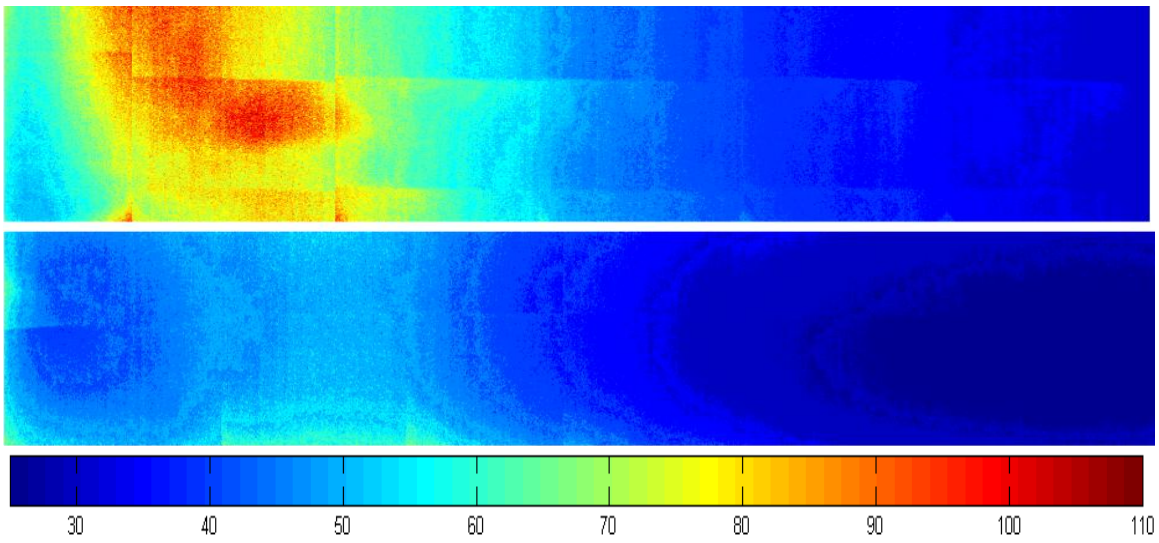

Figure 4.10. Heat transfer coefficient distribution along the concave (top) and convex (bottom) walls for Re = 420,000 with flow direction from left to right (scale in W/m^2K)

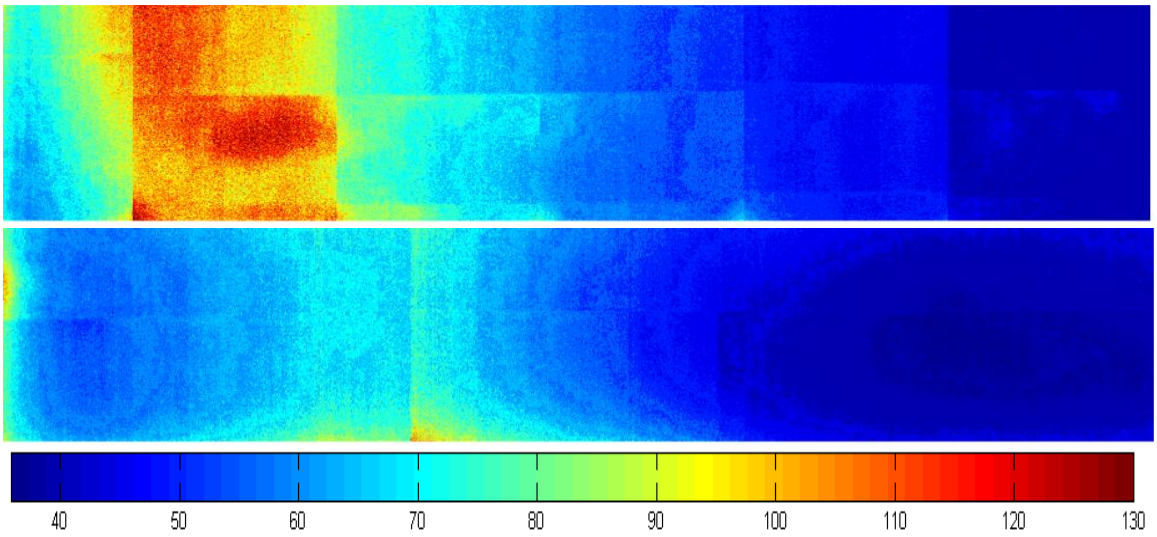

Figure 4.11. Heat transfer coefficient distribution along the concave (top) and convex (bottom) walls for Re = 840,000 with flow direction from left to right(scale in W/m^2K)

The wall sections observed in Figures 4.9-4.11 are approximately 12-cm tall sections that are aligned with the centerline of the middle swirler. From Figures 4.9-4.11, it is clear that there is a significantly larger level of heat transfer along the concave walls of the combustor. The peak heat transfer locations for the concave wall correspond to where the flow exiting the swirler impinges on the wall. This is not the case however, for the convex wall. The impingement location on the convex wall shows only a slight increase in heat transfer and shifts further downstream as the Reynolds number is increased. It appears that the peak heat transfer region on the convex wall lies above and below the impingement region. Without PIV or CFD providing flow visualization, it is difficult to pinpoint the exact reason for this occurrence. However, a basic understanding aerodynamics of swirling flow may provide a good idea of why these trends are seen. Figure 4.12 shows a diagram of how the interaction between the rotating flow generated by the swirlers could impact the wall heat transfer distributions.

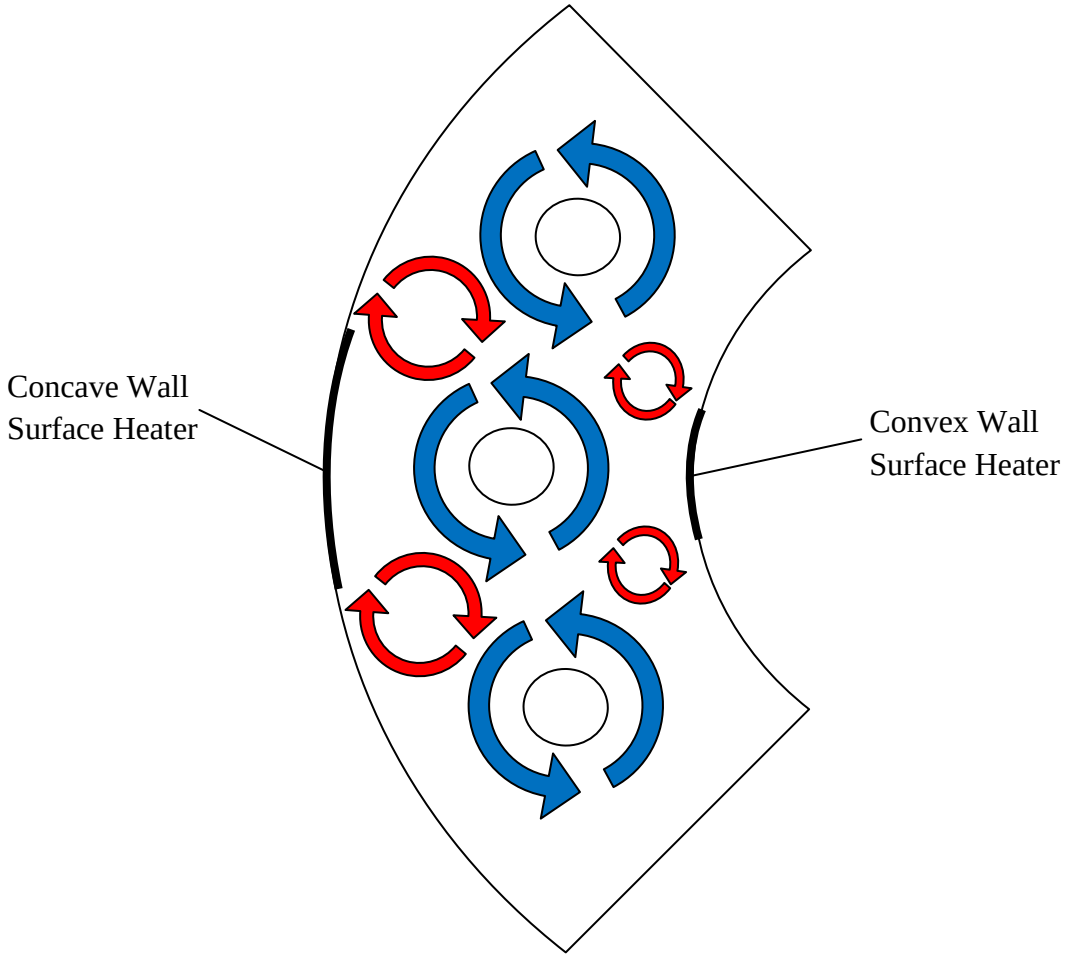

Figure 4.12. Diagram of swirler interaction

Figure 4.12 shows how the rotating flow from the three swirlers in the quarter annulus test section will interact as they enter the combustor. The blue arrows represent the room temperature air exiting the swirlers with a counterclockwise rotation. The red arrows are the recirculation zones that will form as a result of the interaction between the flows from the multiple swirlers. The recirculation zones on the concave wall will be larger than on the convex wall, but will have less turbulent intensity due to the larger area. The highly turbulent recirculation zones on the convex wall can most likely be the cause for why peak heat transfer regions are seen above and below the impingement area.

The large band of downward sloping peak heat transfer seen in the concave wall heat transfer distributions can also be explained from Figure 4.12. With less turbulent recirculation zones along the concave wall, the dominating factor for heat transfer augmentation is the impingement area. Figures 4.9-4.11 show that the center of the impingement region is in fact the area with the largest convective heat transfer for the concave wall. This downward sloping profile can be attributed to the rotational directions of the flow from the swirler. Since the flow is leaving the swirler in a counterclockwise direction, the upper portion of the flow will impact the wall at a much steeper angle closer to perpendicular to the wall. The lower portion of the flow will have a much lower impingement angle and therefore does not produce the larger levels of heat transfer seen in the upper half of the profile.

The Nusselt number along the centerline of the heated area was also computed. The distributions of the Nusselt number along the concave and convex walls are shown in Figures 4.13 and 4.14 respectively. It can be seen that both walls very rapidly reach their peak Nusselt number and begin to decay further down the test section. As expected, the higher Reynolds numbers produce larger Nusselt numbers. For the convex wall, the Nusselt number distribution increases evenly as the Reynolds number is increased. The concave wall shows large gains in the Nusselt number when the Reynolds number is increased from 210,000 to 420,000, but shows little difference between the 420,000 and 840,000 cases.

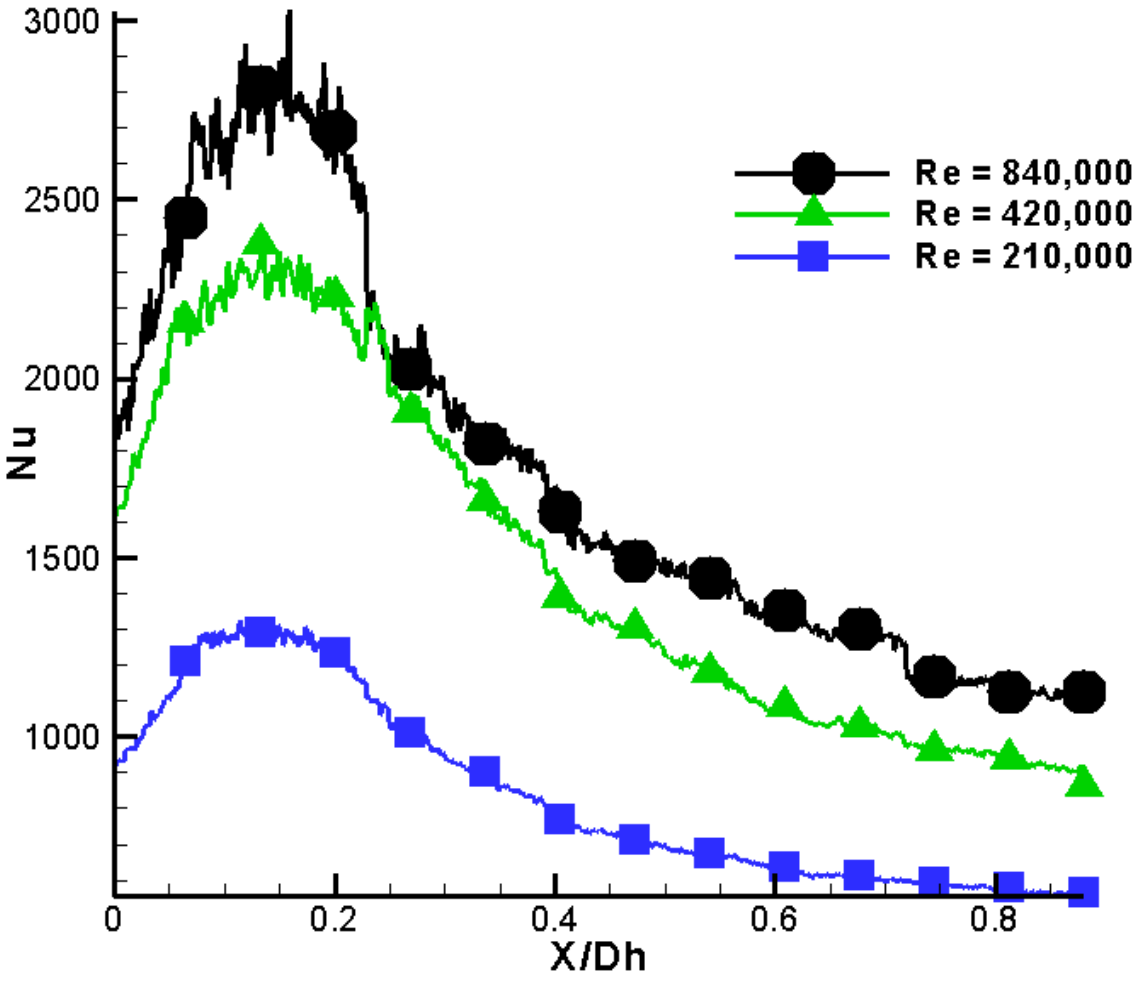

Figure 4.13. Nusselt number distribution along concave combustor wall with reference to combustor diameter at Re=210,000, Re=420,000, and Re=840,000

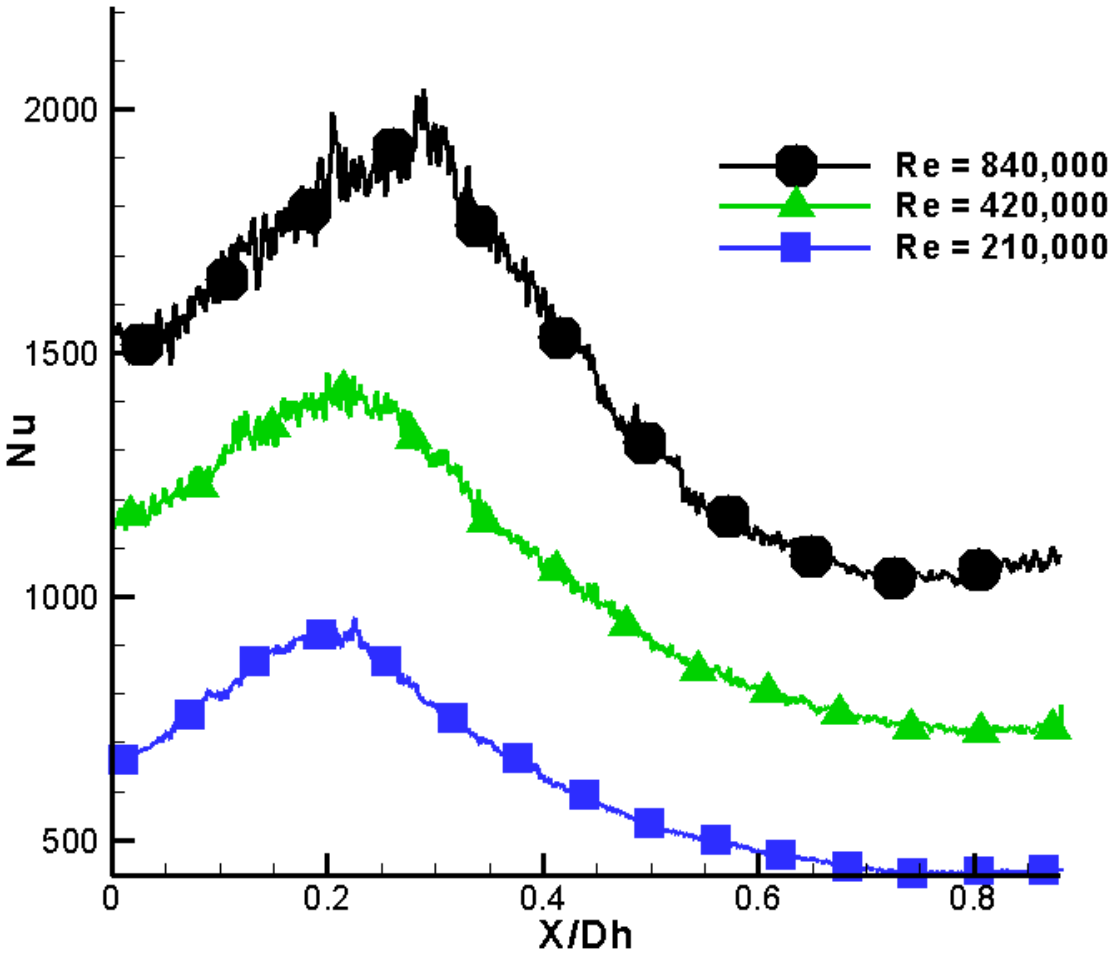

Figure 4.14. Nusselt number distribution along convex combustor wall with reference to combustor diameter at Re=210,000, Re=420,000, and Re=840,000

A comparison of the concave and convex wall Nusselt number distributions is shown in Figure 4.15 for the Reynolds number of 420,000. Figure 4.15 shows that a much larger Nusselt number is seen on the concave wall than the convex wall. The peak locations for the convex wall is also located further downstream than the convex wall.

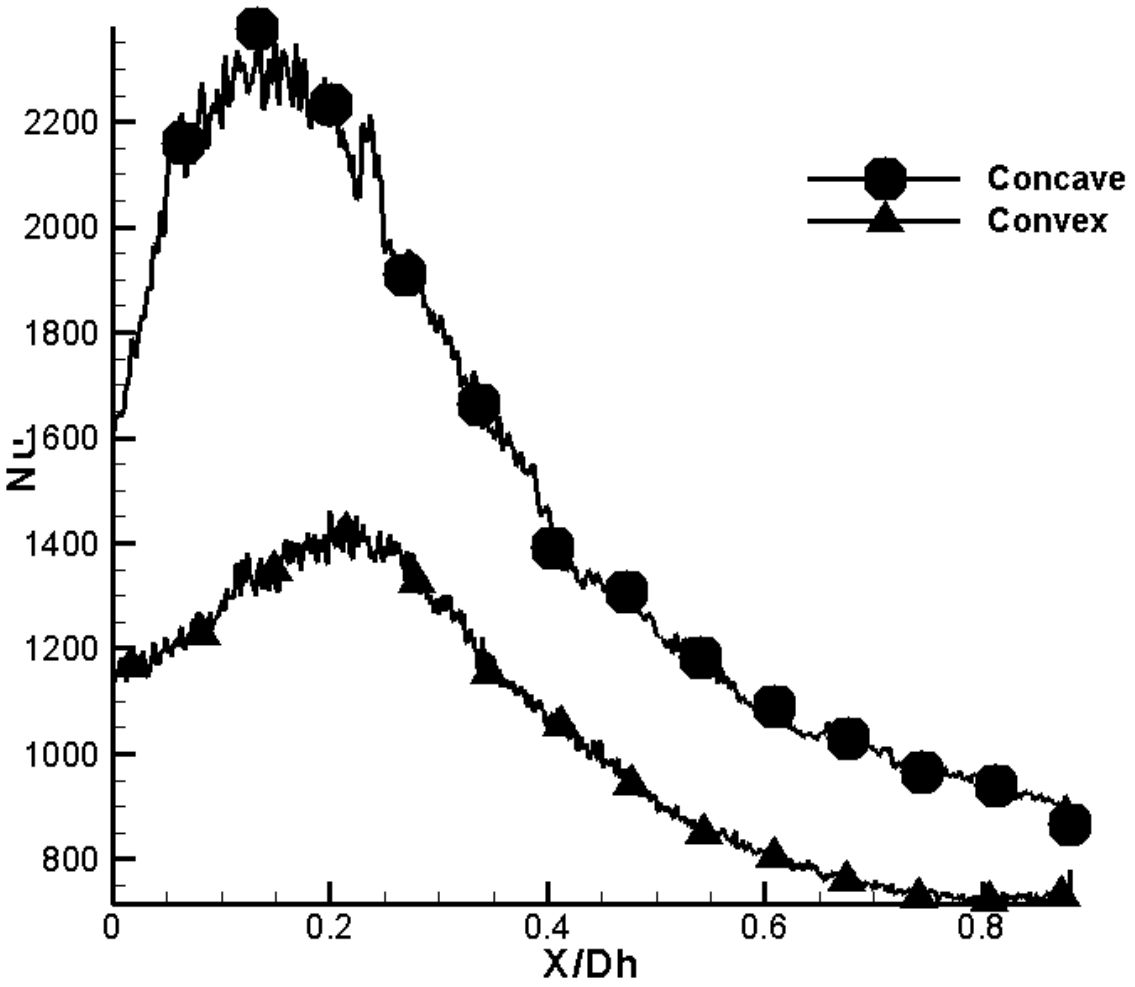

Figure 4.15. Nusselt number distribution comparison between concave and convex combustor walls with reference to combustor diameter at Re=420,000

CHAPTER 5: SUMMARY AND CONCLUSIONS

Flow visualization was performed using PIV to measure axial and radial velocity distributions in a 1:1 scale combustor model at cold flow conditions. Seeding particles were injected into the mainstream airflow through the inlet of the blower. Double frame images were taken at four locations along the axial plane as well as at four radial plane locations and velocities were computed using an adaptive correlation. Measurements show that both swirlers produce a high degree of rotation that causes a reverse core flow inside the can combustor. The radial swirler design produces larger radial velocities than the axial swirler, however the axial swirler has a much more uniform radial velocity distribution.

Steady state heat transfer coefficient distributions along the can combustor wall were also computed using temperature measurements obtained from an IR camera. Surface heaters were placed along the wall to create a constant heat flux to the wall. Flow enters the combustor at cold flow conditions where it interacts with the heated wall sections. Peak heat transfer regions directly correspond to the areas where the flow exits the swirlers and impinges on the combustor wall. The greater mixing in the radial swirler causes the steady state heat transfer measurements to be lower than those produced by the axial swirler.

The steady state heat transfer coefficient was also measured on the concave and convex walls in a 2:1 scale annular combustor fitted with radial swirlers, for Reynolds numbers 210000, 420000, and 840000. Peak heat transfer regions for the concave wall directly correspond to the impingement of the flow from the swirler. The convex wall showed much lower heat transfer distributions with peak levels above and below the

impingement region. This is due to the recirculation zones caused by the interaction between the multiple swirlers inside the annulus.

REFERENCES

[1] Goh, Y., "Heat transfer and flow characteristics inside a gas turbine combustor", MS thesis, Department of Mechanical Engineering, Louisiana State University, 2006.

[2] Lefevebre, A. H., "Gas Turbine Combustion", Taylor & Francis, 2nd Edition, 1998.

[3] Abraham, S., 2008, "Heat Transfer and Flow Measurements on a One-scale Gas Turbine Can Combustor Model," MS thesis, Department of Mechanical Engineering, Virginia Polytechnic Institute and State University, Virginia.

[4] Sedalor, T., 2009, "Heat Transfer and Flow Characteristics in a Low Emission Annular Combustor," MS thesis, Department of Mechanical Engineering, Virginia Polytechnic Institute and State University, Virginia.

[5] Pritchard, B.A., Jr., Danis, A.M., Foust, M.J., Durbin, M.D., Mongia, H.C., 2002, "Multiple Annular Combustion Chamber Swirler Having Atomizing Pilot," U.S. Patent Number 6381964

[6] Graves, C.B., 1999, "Radial Inlet Swirler with Twisted Vanes for Fuel Injector," U.S. Patent Number 5966937

[7] Auer, M.P, Hirsch, C., Sattelmayer, T., 2005, "Influence of the Interaction of Equivalence Ratio and Mass Flow Fluctuations on Flame Dynamics," ASME Paper GT-2005-68373

[8] Xu, G., Cui, Y., Yu, B., Lei, Y., Nie, C., Xiao, Y., Huang, W., 2005, "Design and Development Test of a Gas Turbine Combustor for High Hydrogen Medium Heating Value Syngas Fuel," ASME Paper GT-2005-68567

[9] Phil T. King, Hisham S. Al Kabie, Gordon E. Andrews, Mohamed M. Pourkashanian and Andy C. McIntosh, 2009, "CFD Predictions of Low NOx Radial Swirlers with Central Fuel Injection," ASME Paper GT-2009-60106

[10] Phil T. King, Gordon E. Andrews, Myeong N. Kim, Mohamed Pourkashanian and Andy C. McIntosh, 2009, "CFD Prediction and Design of Low NOx Radial Swirler Systems" ASME Paper GT-2009-60107

[11] Andrews, G.E., Kim, M.N., Mkpadi, M.C. and Akande, S.A., 2007, "Liquid Fuelled Low NOx Radial Swirlers with Central Pilot Combustion" ASME Paper GT-2007-27415.

[12] Andrews, G.E., Delgadillo, E.Z., Mkpadi, M.C. and Hayes, G., 2007, "Hydrogen as a Pilot Gas to Improve Power Turndown in Simulated Ultra Low NOx Gas Turbine Combustion," ASME Paper GT2007-27414.

[13] Janus, B., Dreizler, A., Janicka, J., 2005, "Experimental Study on Stabilization of Lifted Swirl Flames in a Model GT Combustor" Flow, Turbulence and Combustion 2005 75: 293–315

[14] Patil, S., Abraham, S., Tafti, D., Ekkad, S., Kim, Y., Dutta, P., Moon, H., Srinivasan, R., 2011, "Experimental and Numerical Investigation of Convective Heat Transfer in a Gas Turbine Can Combustor" ASME J. Turbomach., vol. 133, 011028, January 2011

[15] King, P.T, Escott, N.H, Andrews, G.E, Pourkashanian, M.M., McIntosh,A.C., 2008, "CFD Predictions of Low NOx Radial Swirlers with Vane Passage Fuel Injection with Comparison with Internal Gas Analysis Flame Composition" ASME Paper GT-2008-51138.

[16] Westerweel, J., 2001, “What is PIV?” AHD TU Delft Experimental Fluid Dynamics and Data Interpretation Presentation.

[17] Westerweel, J., 2001, “Interrogation Analysis” AHD TU Delft Presentation